WILEY | Hindawi

Research Article

Comprehensive Analysis and Design of Electrical Power Systems for Nanosatellite Platforms: A Focus on Robust MPPT Control Using Sliding Mode Control Method

Kerrouche Kamel Djamel Eddine [1,2] Wang Lina [1] Seddjar Abderrahmane [2]
Bensaada Messaoud [2] Pedro Henrique de Oliveira Nogueira,[3]
and Kerrouche Mustapha Boualem [4]

[1]*The School of Automation on Science and Electrical Engineering, Beihang University, Beijing 100191, China*
[2]*Satellites Development Center, Algerian Space Agency, Oran, Algeria*
[3]*Astroscale, Oxfordshire, UK*
[4]*University of El Bayadh Nour El Bachir, El Bayadh, Algeria*

Correspondence should be addressed to Wang Lina; wangln@buaa.edu.cn

This paper is aimed at performing a comprehensive review of the approaches employed in nanosatellite platforms, specifically 1 U and 3 U, for electrical power systems (EPS). Moreover, it seeks to develop a robust maximum power point tracking (MPPT) controller using the sliding mode control (SMC) method. The proposed control strategy is intended to monitor the solar panel's maximum power point (MPP) and adapt to changes in temperatures and solar irradiance in low Earth orbit (LEO). The EPS model, designed with the proposed sizing method, is built in MATLAB-Simulink and integrates a solar panel, battery storage, and power converters controlled by diverse MPPT methods. Then, simulation results demonstrate the effectiveness of the proposed SMC approach compared to other conventional control methods for the designed EPS under varying LEO conditions. To achieve a robust validation of the most appropriate MPPT control method under steady-state conditions, this paper presents an experimental investigation into the proposed EPS hardware design. The proposed SMC method achieved an increase in power generation from 10% to 12% for buck and boost power converters, respectively, compared to traditional control methods.

1. Introduction

Heidt et al. put forth the idea for CubeSat, which was developed through cooperation between Stanford University and California Polytechnic University (Cal Poly). It was created to satisfy the demand for a satellite that could be created in less than two years, at a very low cost, and with little weight to save launch costs [1].

The physical definition of a CubeSat is a cube with a volume of no more than 1.33 kg and dimensions of $10 \times 10 \times 10$ cm. Although more recently, units as tiny as 0.5 U, 1.5 U, 2 U, and 3 U, as shown in Figure 1, and as large as 6 U and 12 U have been added to the CubeSat's dimensions based

on new designs, this design primarily applies to a 1 U Cube-Sat. Producers of satellites might then expand the adaptability and capacity of their products. There is an increase in mass based on the increment of the unit that a satellite was built. The weight of the CubeSat design is 2.66 kg for the 2 U, 3.99 kg for the 3 U, and so forth. These tiny nanosatellites can be launched in large numbers and are less expensive to deploy. Numerous commercial, academic, and other ventures have been sent into orbit as a result of nanosatellite development over time. From the database provided by Kulu [2], illustrated in Figure 2, the most common types of launched nanosatellites are those based on the 3 U and 1 U nanosatellite platforms, indicating broad market and
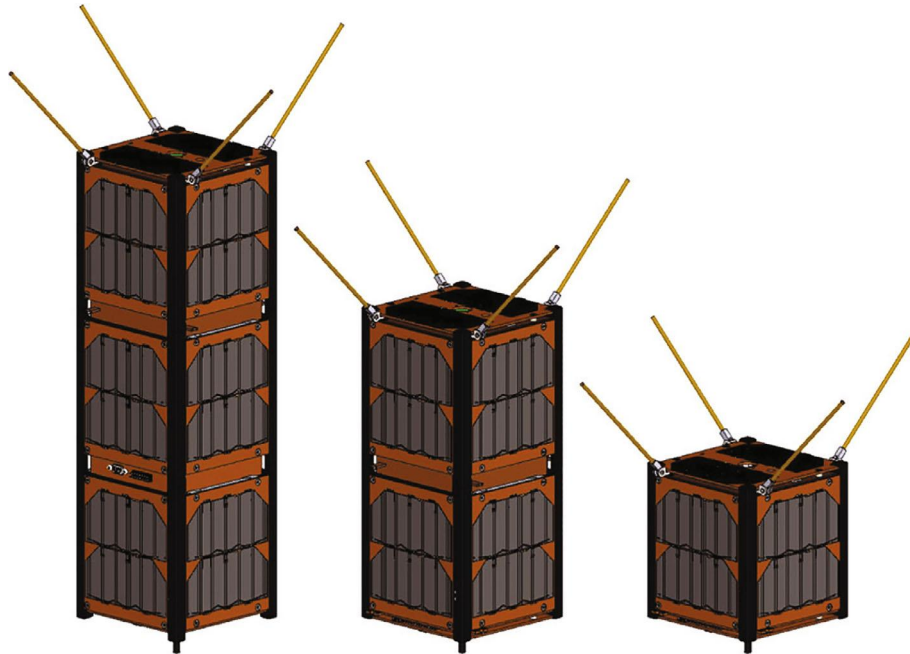
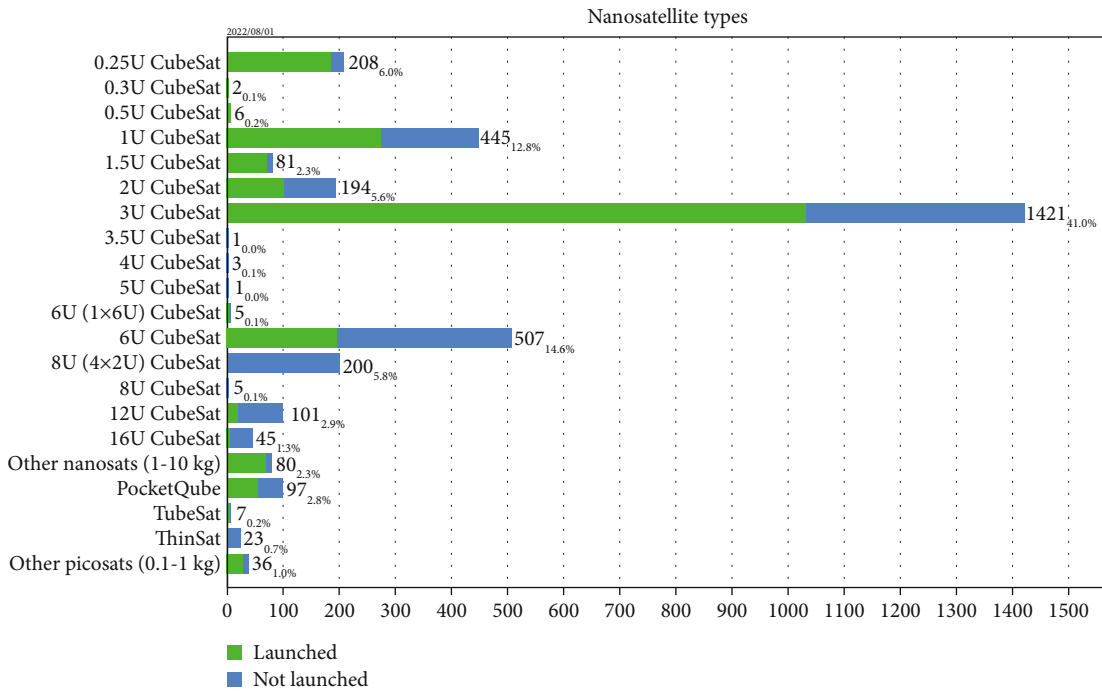FIGURE 1: Nanosatellite platforms: 3 U, 2 U, and 1 U [3].

FIGURE 2: Classes of launched nanosatellites [2].

industry adoption of CubeSat standards. As a result, new businesses like Clyde-Space, EnduroSat, and GOMspace were created to develop and market nanosatellite hardware. These businesses can use the nanosatellite design to supply the entire nanosatellite with the requirements of a certain mission, or they can just supply specific parts, such as solar panels or the structure of the nanosatellite, or even electrical modules like payloads, communication systems, and electrical power systems (EPSs).

What is currently available in terms of EPS development is shown by many recent research studies. In the demonstration of a modular EPS for small satellites, Lim et al. [4] examined operational difficulties and control problems and recommended more studies into EPS design. Johnston-Lemke et al. [5] made a modular, scalable, and efficient EPS that can be mounted on satellites to handle power requirements ranging from 1 W to 1 kW. A way of sizing the vital parts of the EPS, such as the PhotoVoltaic (PV)

solar panels and the batteries, is detailed in Khan et al. [6] and presents a comprehensive design and control strategy for EPS of small satellites. The following elements are taken into account in the enhanced design: PV cell properties, PV panel sizing, storage system requirements, and EPS efficiencies.

The design of EPS begins with determining the amount of power required to supply the nanosatellite's systems, selecting a reliable circuit topology, and choice of a suitable control strategy. The power control stage in small satellites is classified into two types: direct energy transfer (DET) circuits and peak power transfer (PPT) topologies, which are based on an unregulated or regulated bus voltage [7, 8]. The EPS architecture used in nanosatellite based on DET are dissipative methods and without the capability of tracking the maximum power [9]. The DET circuit is the source of theoretically higher losses at the filtering components and dissipative circuit. Nonetheless, the common EPS of nanosatellites using the DET circuit has a problem of efficiency loss. The operation of the solar panel at the maximum power point (MPP) appears to be the worthwhile solution in real low Earth orbit (LEO) conditions, where the nanosatellite's angle toward the sun continuously changes and the total solar irradiance incoming to solar panels varies significantly. The PPT is a nondissipative circuit because it can harvest the precise power needed by the nanosatellite up to the maximum power of the solar array [10]. The control algorithm used for PPT circuit topology is called maximum power point tracking (MPPT), which was integrated into ESTCube-1 into its EPS to optimize the produced energy of the nanosatellite under different space conditions [11]. This strategy increases effectiveness while simultaneously avoiding potential thermal dissipation issues that are present in the DET circuit. A power regulator of this approach is frequently utilized to power both the loads and the batteries [12, 13].

To track the MPP, it is crucial to develop and implement a control algorithm for the PV system. Perturb and Observe (P&O) and Incremental Conductance (INC) approaches are two of the MPPT methods that are available in many research papers [14–16]. These methods work poorly in environments that are changing quickly, even though they are precise and straightforward [17, 18]. The last two decades have seen the proposal of numerous MPPT approaches, including adaptive and enhanced P&O methods [19–21]. Improved techniques of INC methods are presented in [22–24]. Fractional short circuit current (FSCC) techniques are presented in [25, 26], and the FSCC implementation under dSPACE hardware is discussed in [27]. The fractional open circuit voltage (FOCV) technique for maximization of the power produced by the solar system is described in [28], where the enhanced version of FOCV is suggested in [29].

Fractional nonlinear synergetic control (FNSC) for the MPPT method is suggested in [30], and model predictive control (MPC) is proposed in [31]. Intelligent approaches such as the fuzzy logic controller (FLC) theory are presented in [32, 33], where [34] describes how it was implemented on DSP. Artificial neural network (ANN) methods are pre-sented in [35, 36]. Adaptive neuro-fuzzy interference system (ANFIS) and genetic algorithm (GA) approaches are suggested in [37]. The particle swarm optimization (PSO) technique is presented in [38], where it has been also experimentally implemented in [39]. Performance criteria including complexity, convergence rate, speed, soft cost, sensor required, and dependability can all be taken into consideration when selecting one of these MPPT methods. A classification is presented in [40] based on tracking parameters, i.e., constant parameters, measurement comparison, trial and error, a mathematical calculation, and intelligent prediction. MPPT approaches, in general, provide a positive or negative reference signal based on the operational condition of PV systems. Most techniques are robust and accurate under steady conditions but deteriorate when the climatic or loading parameters change abruptly.

The sliding mode control (SMC) method is very precise and notably robust to external and internal perturbations for both linear and nonlinear systems [41–45] and appears to be a suitable control strategy even for MPPT [46]. Studies on SMC, which are based on the inclusion of conventional P&O algorithms, have been published in the literature [47, 48]. These techniques generate the input current reference by using a voltage controller as the sliding surface's base. This becomes problematic since the tracking for the MPP is established by the P&O algorithm, which is used both ways; hence, the technique continues to trade off precision and dynamic reaction. The first-order SMC is recognized as a reliable control approach, even in the absence of the P&O algorithm. Hence, as an alternative method to optimize power in an EPS, under dynamic conditions such as variations in solar irradiance due to orbit changes, this strategy is selected for this research.

Several comprehensive literature reviews have thoroughly investigated and compared the efficiency of PV systems under uniform and nonuniform solar irradiation circumstances [49, 50], and including the analysis of shadow impacts [51]. However, the influence of shadow effects in space, particularly in LEO applications, is negligible. In simulations, the proposed assessment of MPPT controllers primarily focuses on scenarios that closely resemble space conditions to assure the relevance and applicability of the findings to space-based applications. This practice extends a range of conditions, taking into account changes in solar irradiance and temperature, scenarios where the sun is constantly pointed toward, and situations where the irradiance has nonuniform variations.

The proposed research continues with a study of EPS configurations and MPPT control techniques from the perspective of the nanosatellite platforms and the LEO space environment. The main objective of the paper's contribution is the development of the robust control algorithm for MPPT implemented on the EPS used for 1 U and 3 U nanosatellite platforms. In the proposed robust control method, the SMC theory is selected, for its excellent static and dynamic performance (stability and accuracy), and to obtain an acceptable response time without overshoot or ripples. These types of control theories also give better tracking and almost total rejection of the disturbance whatever the
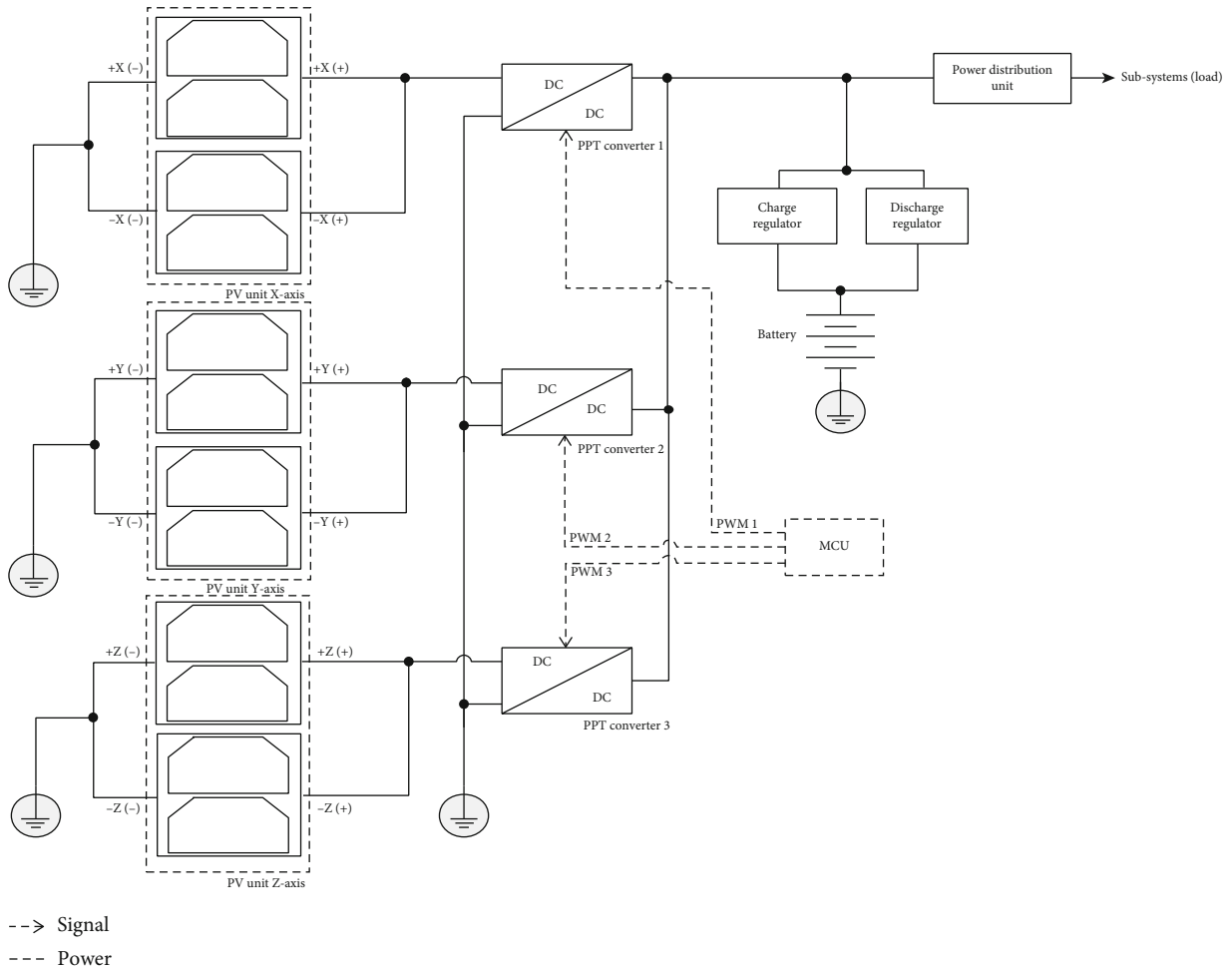
FIGURE 3: Proposed EPS configuration for 1 U nanosatellite with open solar panels' structure.

ranges of variation of the meteorological parameters (temperature and irradiance), and the responses are more stable, more precise, and robust.

The rest of this paper is divided into the following sections: Section 2 will cover nanosatellite EPS configurations and modeling for both 1 U and 3 U nanosatellite platforms. The concise, detailed review of MPPT algorithms used in EPS architectures is presented in Section 3 with the main focus on the design of the proposed SMC method. Some results of the simulation contrasting the proposed SMC method with the conventional MPPT techniques based on P&O and INC are presented in Section 4. Then, experimental results obtained by testing the proposed EPS with MPPT methods are presented in Section 5. A brief conclusion will then be used to conclude this paper.

2. Electrical Power System of Nanosatellites

In the proposed nanosatellite EPS, as shown in Figures 3 and 4, the solar panels are placed on six sides. For the 1 U nanosatellite platform, this will involve three boost power converters for every two solar panels. However, for the 3 U nanosatellite platform, three buck power converters and one boost power converter for every two solar panels are

required. The power converters can be connected in parallel, and each power converter has an inbuilt MPPT. These solar panels are connected on opposing faces of the nanosatellite connected to the same power converter (–X and +X solar arrays are connected to MPPT1, -Y and +Y solar arrays to MPPT2, and –Z and +Z solar arrays to MPPT3). This electrical architecture is highly beneficial since it allows MPPT control of individual solar panels, which have varying MPPs due to irradiance and temperature variances. Instead of employing one boost converter per side of the nanosatellite, one boost power converter can be used for two solar panels on opposite sides of the nanosatellite.

2.1. Photovoltaic System. To extract the maximum sunlight power, efficient PhotoVoltaic (PV) solar cell technology based on triple junction cells is more suitable for nanosatellite applications. This technology involves the deposition of various semiconductor layers, resulting in many subcells, as shown in Figure 5, each with its unique PN junction shape and gap. Each subcell responds to a spectral band based on the semiconductor materials used. Tunnel junctions split the subcells and allow current to flow between them [52].
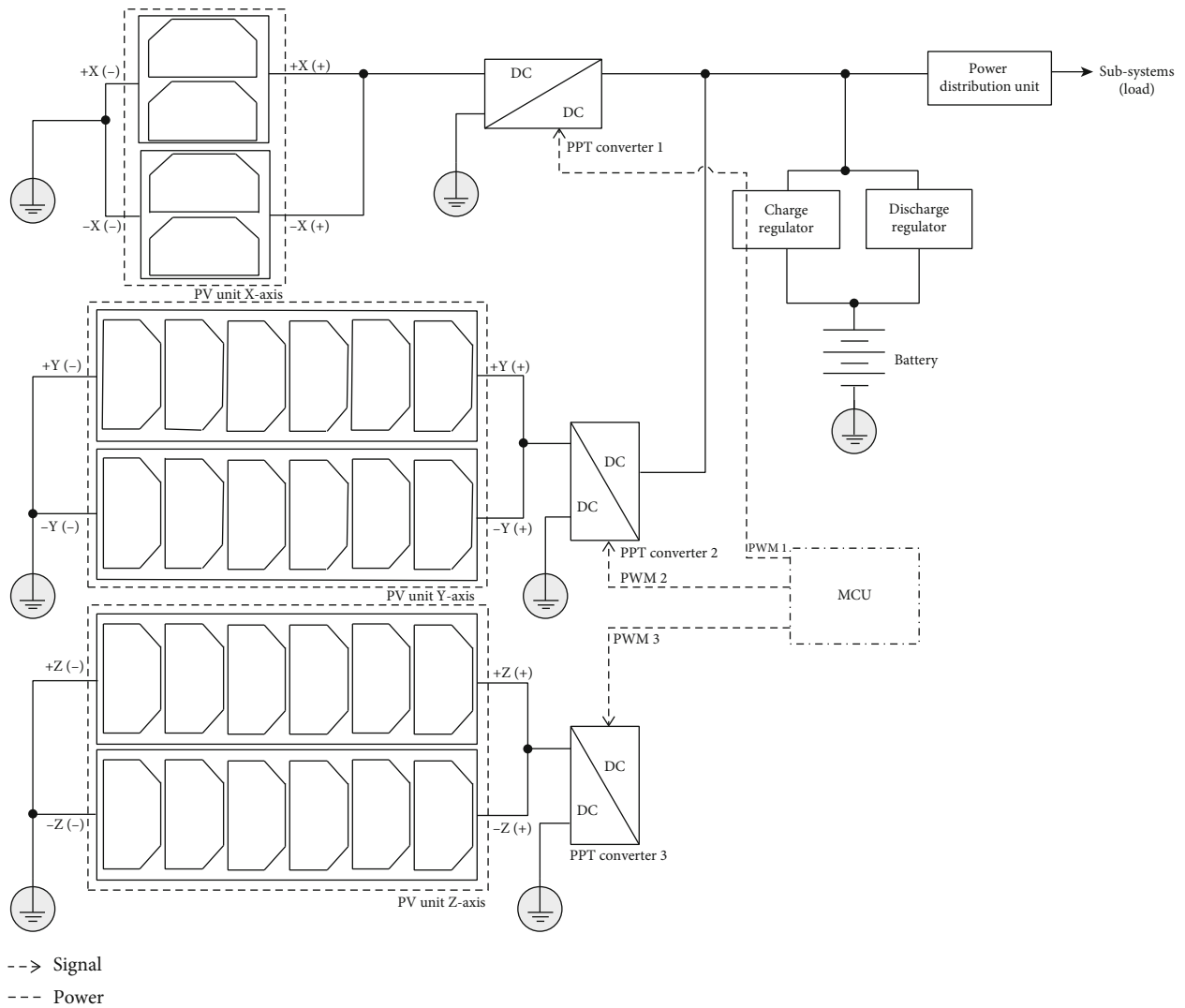
FIGURE 4: Proposed EPS configuration for 3 U nanosatellite with open solar panels' structure.
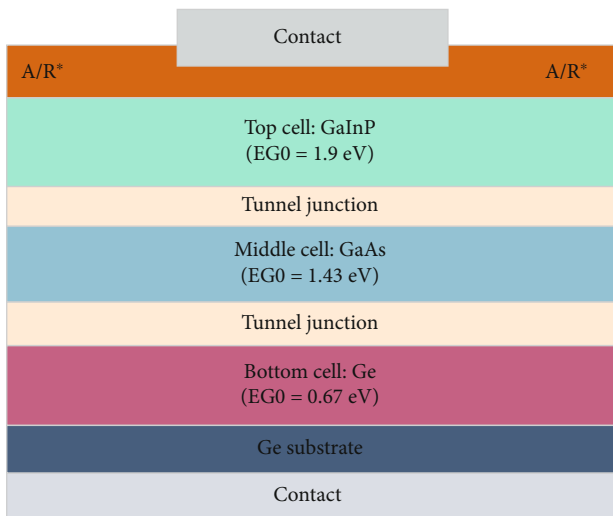

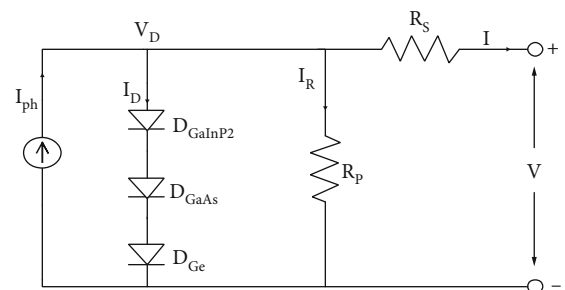FIGURE 5: Structure of triple junction solar cells (InGaP/GaAs/Ge).

FIGURE 6: Triple junction solar cell model.

The circuit shown in Figure 6 provides an equivalent model to understand the electronic behavior of triple-junction solar cells by taking losses linked to manufacturing flaws into account using two resistors (series and shunt). Diodes are used to polarize triple junction cells, resulting in a greater output voltage.

Based on the application of Kirchhoff's law in Figure 6, the following expressions are obtained:

$$I_{ph} = I_D + I_R + I, \qquad (1)$$

where

$$I_D = I_0 \left(e^{q((V+IR_s)/nKT)} - 1 \right), \qquad (2)$$

$$I_R = \frac{V + IR_s}{R_p}, \qquad (3)$$

$$I = I_{ph} - I_0 \left(e^{q((V+IR_s)/nKT)} - 1 \right) - \frac{V + IR_s}{R_p}, \qquad (4)$$

where I_{ph} and I_0 are the PV current and the saturation current of the diode, respectively. The voltage $v_{th} = nKT/q$, and here, K is the Boltzmann constant (1.38×10^{-23} J/K); n is the ideality factor (from 1 to 2); T is the temperature (in kelvin); q is the electron charge (1.6×10^{-19}C).

After simplification ($R_p = \infty$), equation (4) is rewritten as

$$I = I_{ph} - I_0 \left(e^{((V+IR_s)/v_{th})} - 1 \right). \qquad (5)$$

With the consideration of the short circuit ($I_{ph} = I_{sc}$) and the open circuit ($I_{ph} = I_{sc}$) of the solar cells, the following expression is obtained:

$$I_0 = I_{sc} e^{-(V_{oc}/v_{th})}, \qquad (6)$$

where V_{oc} is the open circuit output voltage; I_{sc} is the short circuit output current.

By substituting equation (6) into equation (5) and incorporating the properties of PV cells, a mathematical model for a PV panel is derived:

$$I_{pv} = N_p I_{sc} - N_p I_{sc} \left(e^{((V_{pv} - V_{oc})/N_s v_{th})} \right), \qquad (7)$$

where in the ideal case, R_s is negligible.

The triple-junction solar cells 3G30A technology InGaP/GaAs/Ge selected for the nanosatellite are provided by Azur-Space with an integrated bypass diode. The space-qualified solar cells have an efficiency of 29.5% and an area of 30 cm² and provide 2.7 V of output voltage and 504 mA of output current when the maximum power point is reached [53]. Based on the parameters of AzurSpace solar cells, Figures 7 and 8 show the I-V characteristic PV solar panel in various temperatures under constant solar irradiance, for the two proposed configurations 1 U and 3 U. Whereas, in the same conditions, Figures 9 and 10 present the P-V characteristic of PV solar panels of 1 U and 3 U, respectively.

From the obtained simulation results, it can be concluded that each power versus voltage curve is characterized by a maximum point where the PV panels can generate maximum power. Therefore, this maximum power point (MPP) will change when the temperature T is changing.

2.2. PPT System. A typical configuration of the boost converter connected with the 1 U solar panel is shown in Figure 11.

The dynamical model of the boost DC-DC power converter in state-space form, which is found by the application of basic electricity laws, is written as follows:

$$\frac{dI_l}{dt} = \frac{1}{L} \left(V_{pv} - V_{out}(1 - U) \right), \qquad (8)$$

$$\frac{dI_l}{dt} = \frac{1}{L} \left(V_{pv} - V_{out}(1 - U) \right), \qquad (9)$$

where V_{out} and I_{load} are the output voltage and current, respectively, and V_{pv} is the voltage of the PV panel. The control input $U \in \{0, 1\}$ is the switching function.

Equations (7) and (8) can be written as in-state equation form:

$$\frac{d}{dt} \begin{bmatrix} I_l \\ V_{out} \end{bmatrix} = \begin{bmatrix} 0 & -\dfrac{1}{L} \\ \dfrac{1}{C_2} & -\dfrac{1}{C_2 R} \end{bmatrix} \begin{bmatrix} I_l \\ V_{out} \end{bmatrix} + \begin{bmatrix} \dfrac{V_{out}}{L} \\ -\dfrac{I_l}{C_2} \end{bmatrix} U + \begin{bmatrix} \dfrac{V_{pv}}{L} \\ 0 \end{bmatrix}. \qquad (10)$$

The expressions of the inductor current, the resistance, the inductance, and the capacitances of the input and output capacitors are presented in Table 1, where all expressions are calculated based on a small ripple approximation during a switching period T_s.

The simulation's outcome is depicted in Figure 12. Two graphs of voltages derived from low and high duty cycles are included in this figure, along with two additional graphs of currents obtained from low and high duty cycles. The output voltage is shown on the left axis with a blue solid line, while the current is shown on the right axis with a red dashed line.

The simulation results shown in Figure 12 indicate that the currents are around 0.76 A and 0.52 A with low and high duty cycles (8% and 64%), respectively. The voltages are approximately 6 V and 8.4 V with low and high duty cycles, respectively. It can also be seen that the power converter never goes into discontinuous conduction mode due to the absence of overshoots.

Regarding the aforementioned results, it should be noted that the effectiveness of the sizing approach utilized to compute the parameters of the boost power converter provided in Table 1, according to the EPS requirements, was demonstrated by acceptable values in the simulation with low and high duty cycles.

For the 3 U nanosatellite platform EPS, the buck power converter is used, which is capable of producing an average output voltage less than its input voltage. Figure 13 shows the structure of this converter with resistive load R. This down converter consists of DC input voltage, a controlled switch M connected in series with the circuit, inductor L, two capacitors, and diode D.
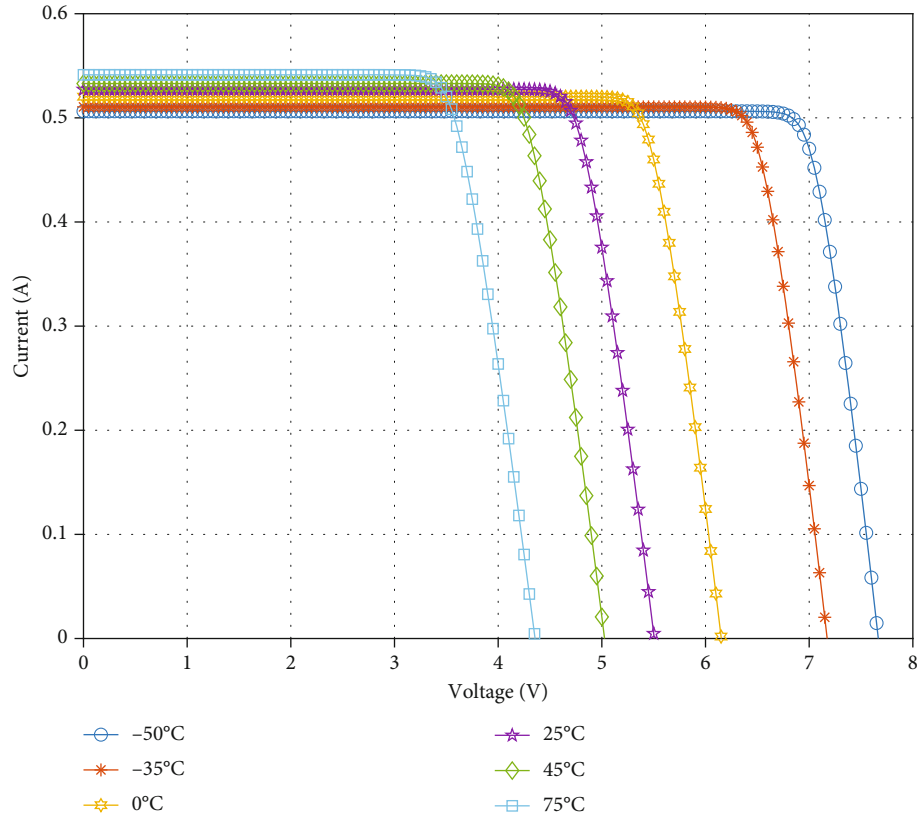
FIGURE 7: Current versus voltage curves of 1 U PV solar panel influenced by temperature variations.

By using fundamental electrical rules, the dynamical model of the buck DC-DC power converter in state-space form may be found as follows:

$$\frac{dI_l}{dt} = \frac{1}{L}\left(UV_{pv} - V_{out}\right),$$ (11)

$$\frac{dV_{out}}{dt} = \frac{1}{C_2}\left(I_l - I_{load}\right),$$ (12)

where V_{pv} is the voltage of the PV panel and V_{out} and $I_{load} = V_{out}/R$ are the output voltage and current, respectively. The control input $U \in \{0, 1\}$ is the switching function.

Equations (7) and (8) can be written as in the following state equation form:

$$\frac{d}{dt}\begin{bmatrix} I_l \\ V_{out} \end{bmatrix} = \begin{bmatrix} 0 & -\dfrac{1}{L} \\ \dfrac{1}{C_2} & -\dfrac{1}{C_2 R} \end{bmatrix}\begin{bmatrix} I_l \\ V_{out} \end{bmatrix} + \begin{bmatrix} \dfrac{V_{pv}}{L} \\ 0 \end{bmatrix} U.$$ (13)

For sizing the buck power converter, the expressions of the inductor current, the resistance, the inductance, and the capacitances of the input and output capacitors are presented in Table 2.

Figure 14 shows the simulation results of the buck power converter based on parameters obtained by both high and low duty cycles, where the right axis depicts currents, while the left axis depicts output voltages.

The simulation results at low and high duty cycles (27% and 88%) are depicted in Figure 14. The voltages are around 6 V and 8.4 V, respectively. The currents are roughly 2.2 A and 1.6 A, respectively. The buck power converter never enters discontinuous conduction mode as a result of no current or their overshoots and ripples passing zero. Likewise, according to the aforementioned findings demonstrated by the simulation with low and high duty cycles, the voltage and current values, as well as their ripples, reached acceptable levels, by the use of the design approach for buck power converter (based on parameters calculated by expressions in Table 2.

3. Maximum Power Point Tracking

For LEO applications, the trend is to optimize numerous existing MPPT techniques, with different degrees of complexity and accuracy [54]. Possibly, the simple tracking method is the perturb and observe (P&O) method which can be implemented in an EPS and can require less computational time and instructions. While, the incremental conductance (INC) method is considered a more complicated method with a slower calculation time (with a large power loss as a consequence [55]), making it a less attractive choice than the P&O.

3.1. P&O Control Algorithm. The P&O control algorithm is often implemented in PV systems used in space applications.
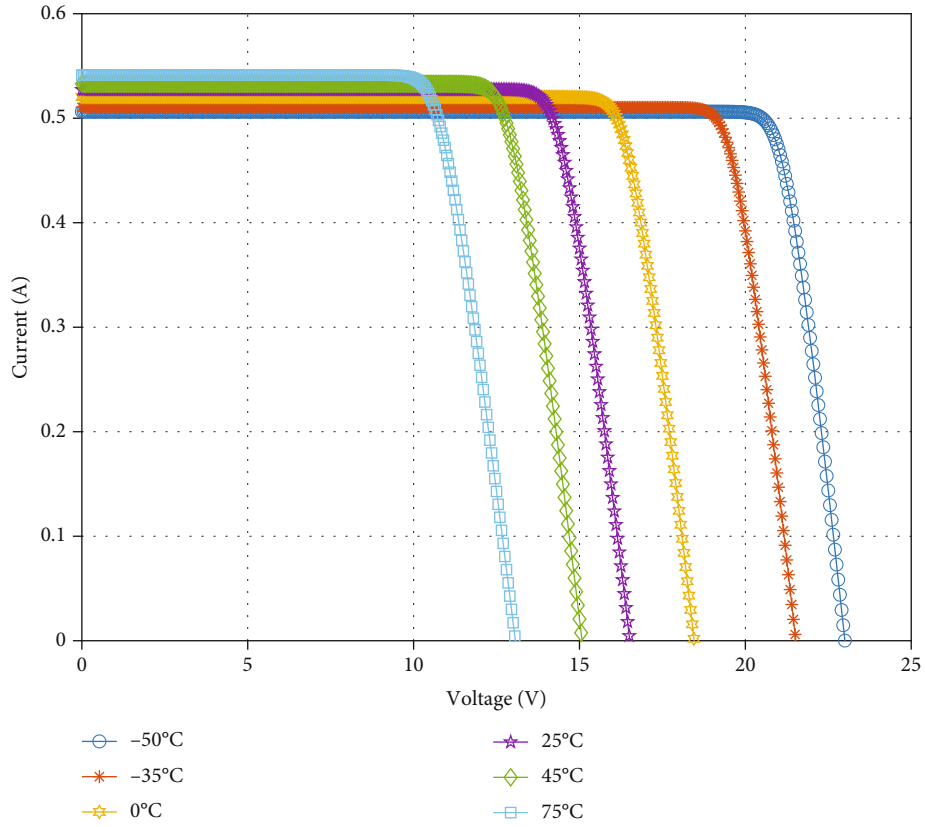
FIGURE 8: Current versus voltage curves of 3 U PV solar panel influenced by temperature variations.
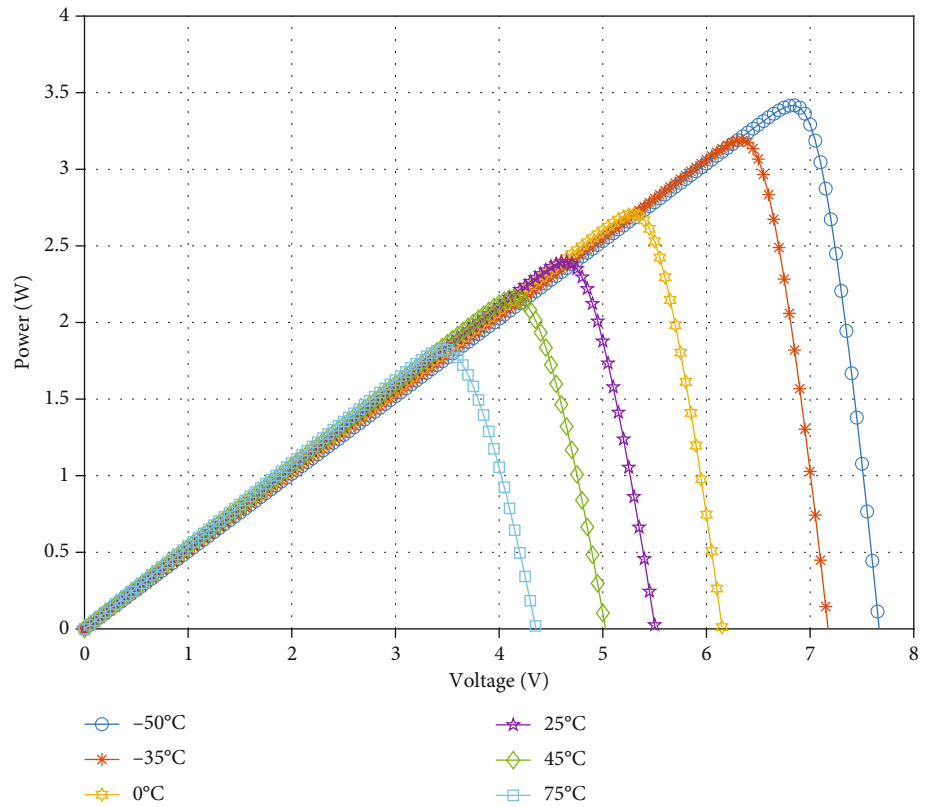

FIGURE 9: Power versus voltage curves of 1 U PV solar panel influenced by temperature variations.
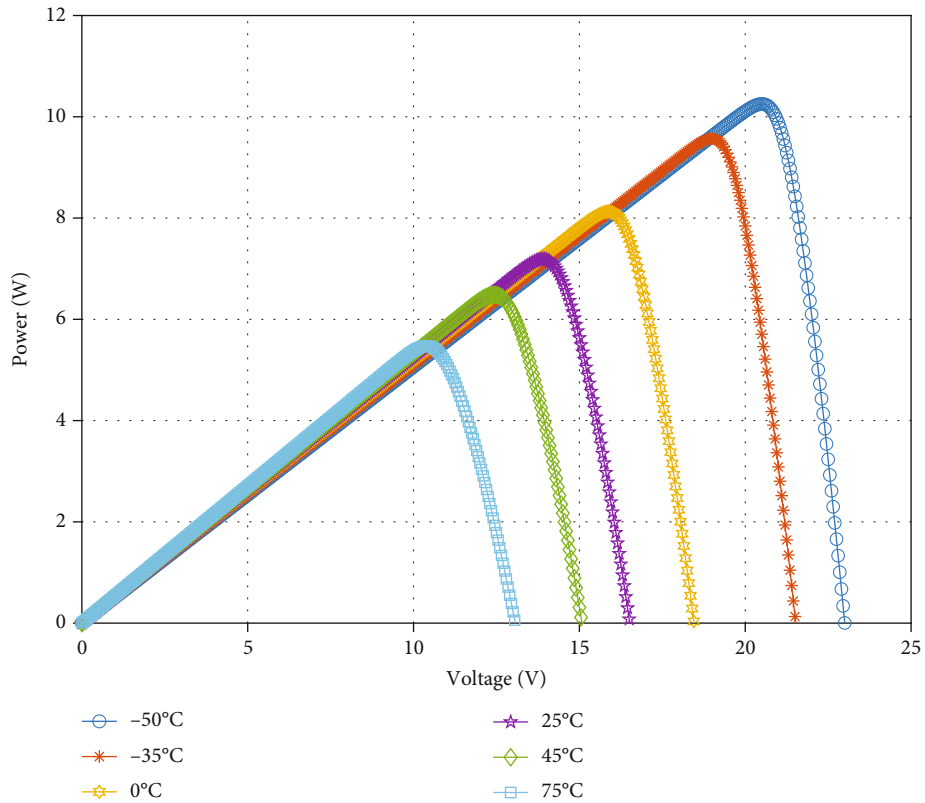
FIGURE 10: Power versus voltage curves of 3 U PV solar panel influenced by temperature variations.
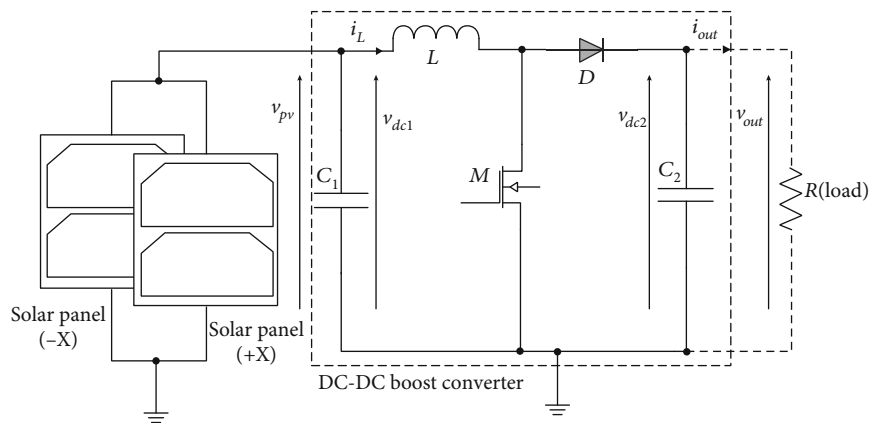

FIGURE 11: Electrical scheme of the boost power converter with 1 U solar panels.

The P&O strategy flowchart is shown in Figure 15, where P, V, and I are the power, voltage, and current, while D represents the duty cycle of the boost control parameter. It has been verified that the P&O technique works well when the irradiance does not vary rapidly with time. On the other hand, the P&O method fails to rapidly follow the maximum power points except if the sampling time and the duty cycle steps are properly chosen [56].

3.2. INC Control Algorithm. The INC approach consists of sensing incremental changes in the current and voltage of the solar panel's outputs to estimate the consequence of these changes on the MPP. When the voltage is changed, this technique employs incremental conductance to calculate the changes in power. As a consequence, the MPP is obtained by the comparison between the variation of the incremental conductance and the conductance of the solar panel. When the difference between the two values is zero, the effective voltage value satisfies the MPP. Therefore, the controller preserves the voltage value until the irradiation or the temperature changes, where the process of measuring and calculating new values is repeated [57]. The INC algorithm flowchart is shown in Figure 16.

Table 1: Boost power converter parameters' expressions for high and low duty cycles.

Low duty cycle	High duty cycle
$D_{\min} = 1 - \dfrac{V_{pv,\max}}{V_{out,\min}}$	$D_{\max} = 1 - V_{pv,\min}/V_{out,\max}$
$R_{\min} = \dfrac{V_{out,\min}^2}{P_{out}}$	$R_{\max} = V_{out,\max}^2/P_{out}$
$I_L = \dfrac{V_{out,\min}}{R_{\min}}\dfrac{1}{1-D_{\min}}$	$I_L = (V_{out,\max}/R_{\max})(1/1-D_{\max})$
$\Delta I_{L,\min} = \dfrac{I_{L,\min}\Delta I_L(\%)}{100}$	$\Delta I_{L,\max} = I_{L,\max}\Delta I_L(\%)/100$
$L_{\min} = \dfrac{1}{2}\left(\dfrac{V_{pv,\max}}{\Delta I_{L,\min}}(D_{\min}T_s)\right)$	$L_{\max} = 1/2\left((V_{pv,\min}/\Delta I_{L,\max})(D_{\max}T_s)\right)$
$\Delta V_{out,\min} = \dfrac{V_{out,\min}\Delta V_{out}(\%)}{100}$	$\Delta V_{out,\max} = V_{out,\max}\Delta V_{out}(\%)/100$
$C_{1,\min} = \dfrac{V_{out,\min}D_{\min}}{8L_{\min}\Delta V_{out,\min}F^2}$	$C_{1,\max} = V_{out,\max}D_{\max}/8L_{\max}\Delta V_{out,\max}F^2$
$C_{2,\min} = \dfrac{V_{out,\min}D_{\min}T_s}{2\Delta V_{out,\min}R_{\min}}$	$C_{2,\max} = V_{out,\max}D_{\max}T_s/2\Delta V_{out,\max}R_{\max}$

3.3. *Sliding Mode Control Algorithm.* A sliding mode control (SMC) theory is a type of variable structure controller (VSC). Unlike continuous functions that can map a plant state to a control surface, a VSC consists of several switching between different functions determined by the plant state characterization [58].

The design of the SMC will be demonstrated for the following nonlinear system [59]:

$$\dot{x} = f(x,t) + B(x,t)U(x,t), \tag{14}$$

where $x \in \Re^n$ is the state vector and $f(x,t)x \in \Re^n$, $B(x,t)x \in \Re^{n \times m}$, and $U(x,t)x \in \Re^m$ are the control vectors.

From equation (12), it is possible to define a set S of the state trajectories x such as

$$S = \{x(t)|S(x,t)=0\}, \tag{15}$$

where

$$S(x,t) = [S_1(x,t), S_2(x,t), S_3(x,t), \ldots, S(x,t)]^T. \tag{16}$$

And $[.]^T$ denotes the transposed vector, and S is called the sliding surface.

To carry the state variable to the sliding surfaces, the following two conditions have to be satisfied:

$$S(x,t) = 0, \tag{17}$$

$$\dot{S}(x,t) = 0. \tag{18}$$

The control law satisfies the precedent conditions that are presented in the following form:

$$U = U_{eq} + U_n, \tag{19}$$

$$U_n = -K_{smc}\,\text{sign}\,(S(x,t)), \tag{20}$$

where U is the control vector, U_{eq} is the equivalent control vector, U_n is the switching part of the control (the correction factor), and K_{smc} is the controller gain. U_{eq} can be obtained by considering the condition for the sliding regime, $S(x,t) = 0$. The equivalent control retains the state variable on the sliding surface, once they achieve it. For the defined function

$$\text{sign}\,(\varphi) = \begin{cases} 1, & \text{if} \quad \varphi > 0 \\ , & \text{if} \quad \varphi = 0 \\ 1, & \text{if} \quad \varphi < 0 \end{cases}. \tag{21}$$

The controller described by equation (19) presents high robustness, insensitive to parameter instabilities, but it will have high-frequency switching (chattering phenomena) nearby to the sliding surface due to the sign function involved by presenting a boundary layer [60].

(19) is rewritten as [61]

$$U = U_{eq} - K_{smc}\,\text{sign}\,(S(x,t)). \tag{22}$$

Consider a Lyapunov function:

$$V(x) = \frac{1}{2}S(x)^2. \tag{23}$$

If the Lyapunov theory of stability is used to ensure that SMC is attractive and invariant, the following condition has to be satisfied:

$$\dot{V}(x) = \frac{1}{2}\frac{d}{dt}S(x)^2 \leq 0. \tag{24}$$

The sliding surface proposed by Slotine and Li [62]

$$S(x) = \left(\frac{\partial}{\partial t} + \lambda_x\right)^{n-1}e(x), \tag{25}$$

where $e(x)$ is the error vector, λ_x is a positive coefficient, and n is the system order.

3.3.1. *Application of the Proposed Sliding Mode Control for Boost Power Converter.* In this paper, the condition of the MPP is given by

$$\frac{dP_{pv}}{dV_{pv}} = 0. \tag{26}$$

For the photovoltaic system, based on condition (26), the sliding surface will be specified as

$$S(x) = \frac{dP_{pv}}{dV_{pv}} = I_{pv} + \frac{dI_{pv}}{dV_{pv}}V_{pv}. \tag{27}$$
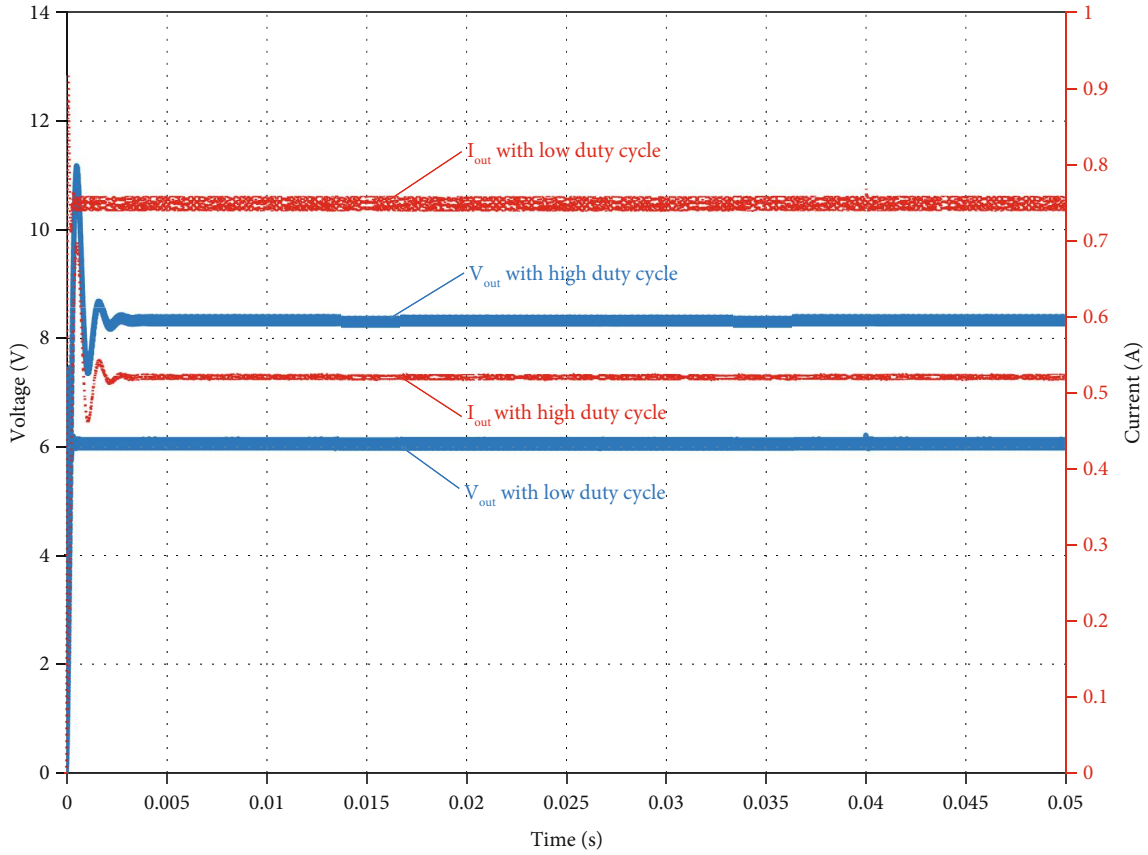
FIGURE 12: Simulation of the buck power converter with high and low duty cycles: dashed red line (output currents) and solid blue line (output voltages).
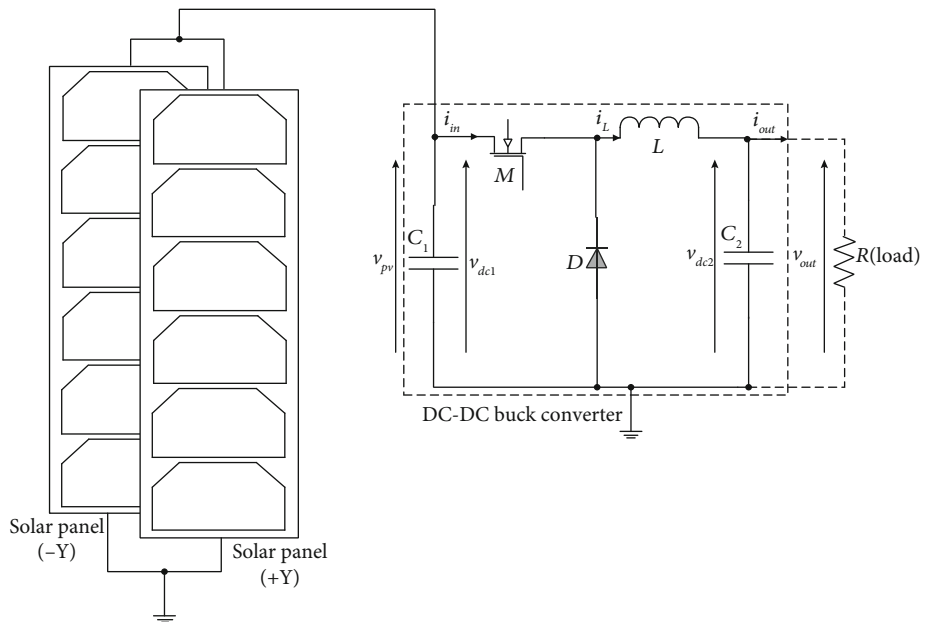

FIGURE 13: Electrical scheme of the buck power converter with 3 U solar panels.

TABLE 2: Buck power converter parameters' expressions for high and low duty cycles.

Low duty cycle	High duty cycle
$D_{\min} = \dfrac{V_{\mathrm{pv,max}}}{V_{\mathrm{out,min}}}$	$D_{\max} = V_{\mathrm{pv,min}}/V_{\mathrm{out,max}}$
$R_{\min} = \dfrac{V_{\mathrm{out,min}}^2}{P_{\mathrm{out}}}$	$R_{\max} = V_{\mathrm{out,max}}^2/P_{\mathrm{out}}$
$I_{L,\min} = \dfrac{V_{\mathrm{out,min}}}{R_{\min}}$	$I_{L,\max} = V_{\mathrm{out,max}}/R_{\max}$
$\Delta I_{L,\min} = \dfrac{I_{L,\min}\Delta I_L(\%)}{100}$	$\Delta I_{L,\max} = I_{L,\max}\Delta I_L(\%)/100$
$L_{\min} = \dfrac{1}{4}\left(\dfrac{V_{\mathrm{pv,max}}}{\Delta I_{L,\min} F}\right)$	$L_{\max} = 1/4\left(V_{\mathrm{pv,min}}/\Delta I_{L,\max} F\right)$
$\Delta V_{\mathrm{out,min}} = \dfrac{V_{\mathrm{out,min}}\Delta V_{\mathrm{out}}(\%)}{100}$	$\Delta V_{\mathrm{out,max}} = V_{\mathrm{out,max}}\Delta V_{\mathrm{out}}(\%)/100$
$C_{1,\min} = \dfrac{\Delta I_{L,\min} D_{\min}}{\Delta V_{\mathrm{pv,max}} F}$	$C_{1,\max} = \Delta I_{L,\max} D_{\max}/\Delta V_{\mathrm{pv,min}} F$
$C_{2,\min} = \dfrac{\Delta I_{L,\min} D_{\min}}{8\Delta V_{\mathrm{out,min}} F}$	$C_{2,\max} = \Delta I_{L,\max} D_{\max}/8\Delta V_{\mathrm{out,max}} F$

To determine the condition of stability on the sliding surface, the notion of equivalent command is used. Using invariance conditions (17), the equivalent command expression can be calculated as proposed by Kerrouche et al. and Brea et al. [63, 64], for the derivative of the sliding mode surface, which is written as

$$\dot{S}(x) = \frac{\partial S}{\partial x_1}\dot{x}_1 + \frac{\partial S}{\partial x_2}\dot{x}_2 = \frac{\partial S}{\partial I_l}\dot{I}_l + \frac{\partial S}{\partial V_{\mathrm{out}}}\dot{V}_{\mathrm{out}}. \tag{28}$$

$S(x)$ is not depending on $\dot{x}_2$, and the following simplifications are obtained:

$$\frac{\partial S}{\partial x_1} \neq 0, \tag{29}$$

$$\frac{\partial S}{\partial x_2} = 0. \tag{30}$$

Applying (29) in (28), the following derivative of the sliding surface is obtained:

$$\dot{S}(x) = \frac{\partial S}{\partial x_1}\dot{x}_1 = \frac{\partial S}{\partial I_l}\dot{I}_l = 0. \tag{31}$$

Therefore, the derivative of the sliding surface is obtained as follows:

$$\dot{S}(x) = \dot{I}_l = 0. \tag{32}$$

From (8) and (32), the following expression is obtained:

$$\frac{dI_l}{dt} = \frac{1}{L}\left(V_{\mathrm{pv}} - V_{\mathrm{out}}\left(1 - U_{\mathrm{eq}}\right)\right) = 0. \tag{33}$$

Subsequently, the expression of the equivalent control applied to the boost power converter is as follows:

$$U_{\mathrm{eq}} = 1 - \frac{V_{\mathrm{pv}}}{V_{\mathrm{out}}}. \tag{34}$$

From (22), the total sliding mode control for the boost power converter becomes

$$U = U_{\mathrm{eq}} + U_n = 1 - \frac{V_{\mathrm{pv}}}{V_{\mathrm{out}}} - K_{\mathrm{smc}} \operatorname{sign}\left(S(x,t)\right). \tag{35}$$

3.3.2. Application of the Proposed Sliding Mode Control for Buck Power Converter. For the photovoltaic system with a buck power converter, the same sliding surface previously used will be defined as

$$S(x) = \frac{dP_{\mathrm{pv}}}{dV_{\mathrm{pv}}} = I_{\mathrm{pv}} + \frac{dI_{\mathrm{pv}}}{dV_{\mathrm{pv}}} V_{\mathrm{pv}}. \tag{36}$$

The derivative of the sliding mode surface is

$$\dot{S}(x) = \frac{\partial S}{\partial x_1}\dot{x}_1 + \frac{\partial S}{\partial x_2}\dot{x}_2 = \frac{\partial S}{\partial I_l}\dot{I}_l + \frac{\partial S}{\partial V_{\mathrm{out}}}\dot{V}_{\mathrm{out}}. \tag{37}$$

$S(x)$ is not depending on $\dot{x}_2$, and the following expression is obtained:

$$\frac{\partial S}{\partial x_1} \neq 0, \tag{38}$$

$$\frac{\partial S}{\partial x_2} = 0. \tag{39}$$

Applying (38) in (37), the derivative of the sliding surface is obtained as

$$\dot{S}(x) = \frac{\partial S}{\partial x_1}\dot{x}_1 = \frac{\partial S}{\partial I_l}\dot{I}_l = 0, \tag{40}$$

where

$$\dot{I}_l = 0. \tag{41}$$

From (8) and (41), the following expression is obtained:

$$\frac{dI_l}{dt} = \frac{1}{L}\left(U_{\mathrm{eq}}V_{\mathrm{pv}} - V_{\mathrm{out}}\right) = 0. \tag{42}$$

So, the expression of the equivalent control applied to the buck power converter is as follows:

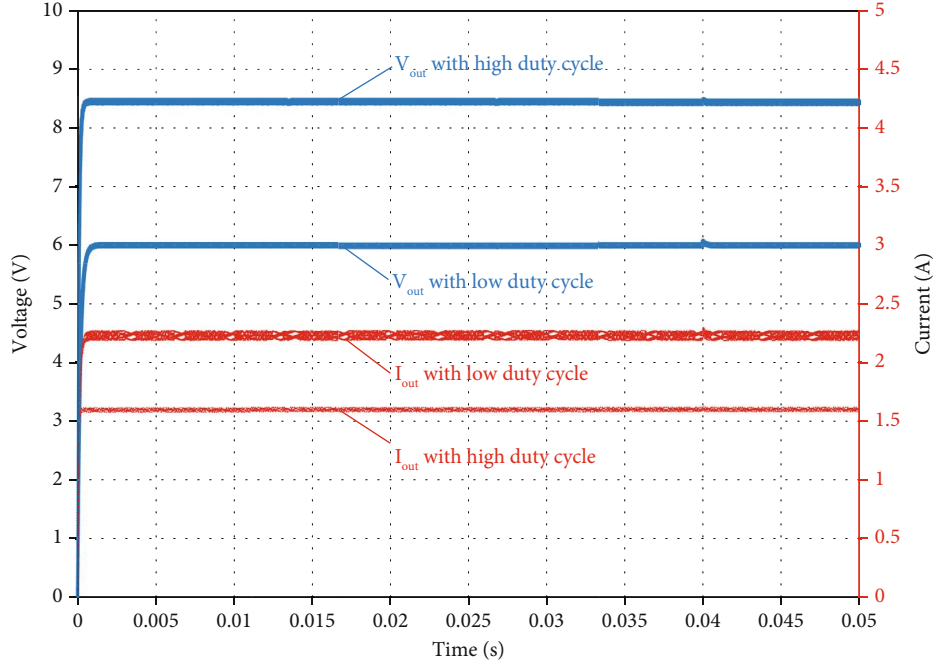$$U_{\mathrm{eq}} = \frac{V_{\mathrm{out}}}{V_{\mathrm{pv}}}. \tag{43}$$

FIGURE 14: Simulation of the buck power converter with high and low duty cycles: dashed red line (output currents) and solid blue line (output voltages).

From (22), the total sliding mode control for buck power converter becomes

$$U = U_{eq} + U_n = \frac{V_{out}}{V_{pv}} - K_{smc} \, \text{sign} \, (S(x,t)). \quad (44)$$

3.3.3. Stability Analysis of the Proposed Sliding Mode Control for Boost and Buck Power Converters. The Lyapunov approach, which is used in this research as well, is frequently used to perform stability analysis for the SMC [65]. Therefore, it is significant to note that the sign of the surface S, as shown in Figure 17, will be utilized in the Lyapunov approach to analyze the stability of the system.

Applying the Lyapunov theorem ensures that the closed-loop system with the SMC guarantees finite-time convergence to the maximum power point. The analysis demonstrates that the sliding surface approaches zero within a finite time, leading to global Lyapunov stability in the system.

To ensure that the surface $S(x) = 0$ is attractive over the entire operating range, it suffices to have the derivative of the Lyapunov function $V(x) = (1/2)S(x)^2$ with respect to time be negative. The following condition is referred to as the attractiveness condition or reachability condition:

$$\dot{V}(x) = \dot{S}(x)S(x) < 0,$$
$$\forall S(x) \neq 0. \quad (45)$$

The sliding surface in (27) can be rewritten as

$$S(x) = N_p I_{sc} - N_p I_{sc} \left(1 + \frac{V_{pv}}{N_s V_{th}} \right) e^{\left((V_{pv} - N_s V_{oc})/N_s V_{th} \right)}. \quad (46)$$

The derivative of the sliding surface can be written as

$$\dot{S}(x) = \frac{\partial S}{\partial x} \dot{x}. \quad (47)$$

After the introduction of sliding surface (46), its derivative is obtained as

$$\dot{S}(x) = \frac{\partial}{\partial x} \left(N_p I_{sc} - N_p I_{sc} \left(1 + \frac{V_{pv}}{N_s V_{th}} \right) e^{\left((V_{pv} - N_s V_{oc})/N_s V_{th} \right)} \right) \dot{x}. \quad (48)$$

Proof.

To establish the existence theorem of the sliding mode, the two zones presented in Figure 17 are considered. By employing equation (27), the derivative of the sliding surface is detailed as follows:

$$\dot{S}(x) = -\left(\frac{V_{pv}}{N_s v_{th}} + 2 \right) \frac{I_{sc}}{N_s V_{th}} e^{\left((V_{pv} - N_s V_{oc})/N_s v_{th} \right)} \frac{dV_{pv}}{dt}. \quad (49)$$

Zone 1. $S(x) > 0$.

If the functioning point is in zone 1, the voltage needs to be increased to reach the MPP. This implies that $(dV_{pv})/dt > 0$. By substituting this into equation (49), where $\dot{S}(x) < 0$ is obtained, it implies $\dot{S}(x)S(x) < 0$.
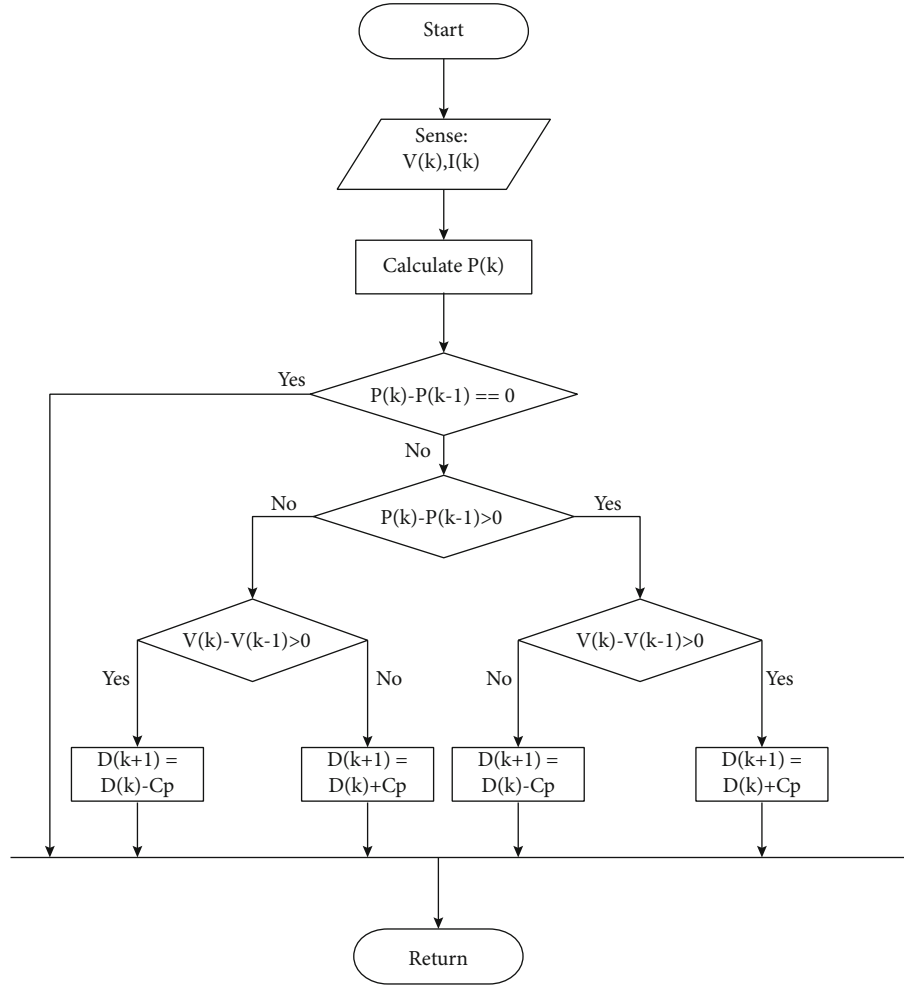
FIGURE 15: Flowchart of P&O MPPT technique.

Zone 2. $S(x) < 0$.

If the system operates in zone 2, the voltage needs to be decreased to reach the MPP. This implies that $dV_{pv}/dt < 0$. By substituting this into equation (49), it follows that $\dot{S}(x) > 0$ which implies $\dot{S}(x)S(x) < 0$.

Based on the above analysis, it can be concluded that the system exhibits sliding mode behavior and is asymptotically stable, regardless of the functioning point's location. The applied control law ensures that the system's trajectory transitions from any initial state onto the sliding surface within a finite time and remains on it thereafter.

Since the range of duty cycle must lie in $0 \leq U_{eq} \leq 1$, the real control signal is proposed as

$$
U = \begin{cases} 0, & \text{for} \quad U_{eq} + U_n \leq 0 \\ U_{eq} + U_n, & \text{for} \quad 0 < U_{eq} + U_n < 1 \,. \\ 1, & \text{for} \quad U_{eq} + U_n \geq 1 \end{cases} \tag{50}
$$

The control input will be taken into account, and several cases will be examined in the stability analysis that follows.

Therefore, the derivative of the sliding surface can also be expressed in the following form:

$$
\dot{S}(x) = \frac{\partial}{\partial I_{pv}} \left(\frac{\partial I_{pv}}{\partial V_{pv}} - \frac{I_{pv}}{V_{pv}} \right) \dot{I}_{pv}. \tag{51}
$$

The derivative of the sliding surface is detailed as follows:

$$
\dot{S}(x) = \frac{\partial}{\partial I_{pv}} \left(\frac{\partial I_{pv}}{\partial V_{pv}} - \frac{I_{pv}}{V_{pv}} \right) \left(\frac{1}{L} \left(V_{pv} - V_{out} \left(1 - U_{eq} - U_n \right) \right) \right). \tag{52}
$$

The first part has the following simplification:

$$
\frac{\partial}{\partial I_{pv}} \left(\frac{\partial I_{pv}}{\partial V_{pv}} - \frac{I_{pv}}{V_{pv}} \right) = \frac{1}{V_{pv}} - \frac{I_{pv}}{V_{pv}^2} \frac{\partial V_{pv}}{\partial I_{pv}} + \frac{N_p e^{(-(V_{oc}/v_{th}))}}{N_s v_{th}} \frac{\partial I_{pv}}{\partial V_{pv}} \frac{\partial V_{pv}}{\partial I_{pv}}. \tag{53}
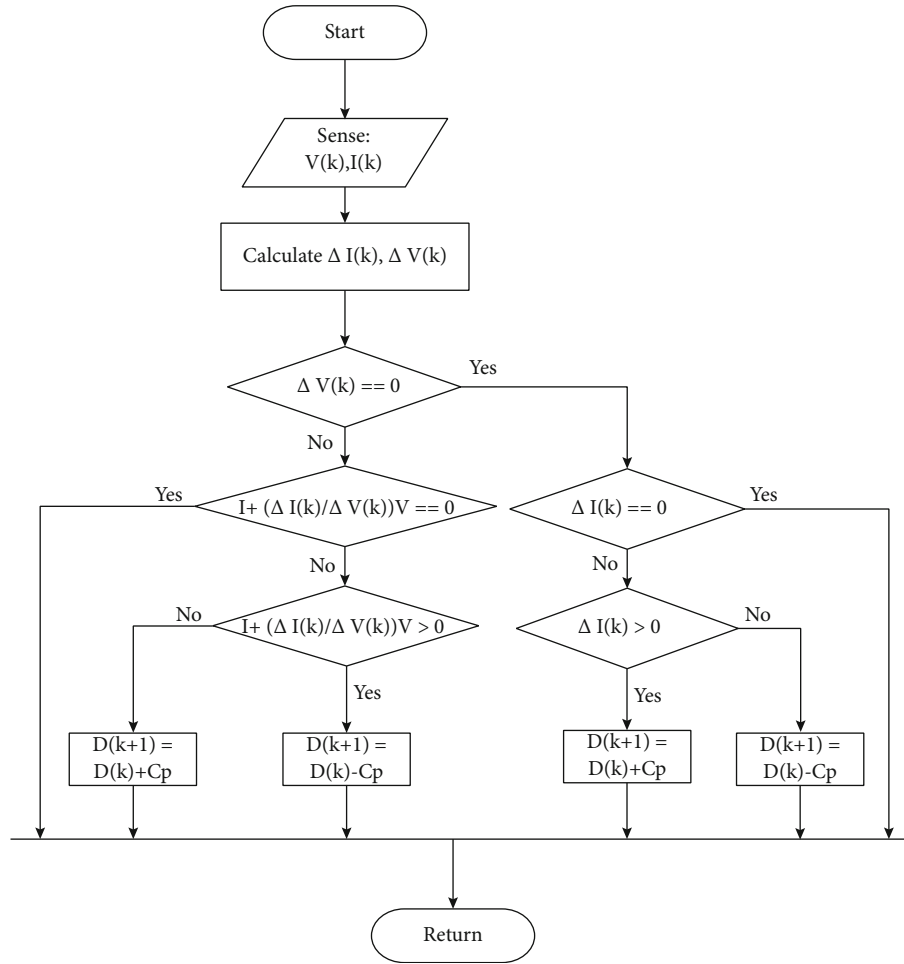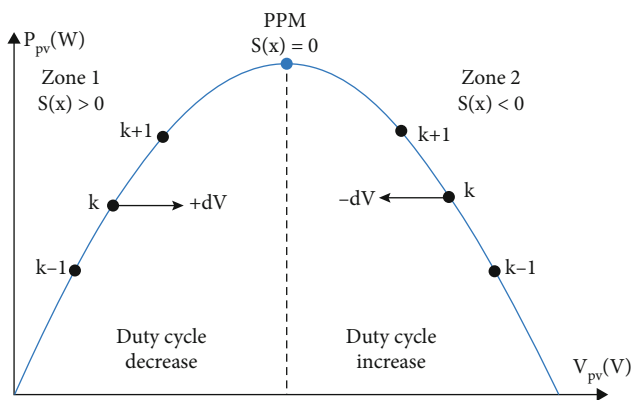$$

FIGURE 16: INC MPPT algorithm flowchart.

FIGURE 17: Control law evolution based on the sign of the surface.

The first term of the sliding surface derivative, which is the derivative of the PV current, is defined as

$$\frac{\partial I_{pv}}{\partial V_{pv}} = -\frac{N_p I_{sc}}{N_s v_{th}} e^{\left(\left(V_{pv} - N_s V_{oc}\right)/N_s v_{th}\right)} < 0. \tag{54}$$

Referring to (7), the PV voltage can be rewritten as

$$V_{pv} = N_s v_{th} \ln\left(\frac{N_p I_{sc} - I_{pv}}{N_p I_{sc}}\right) + N_s V_{oc}. \tag{55}$$

The first derivative of the PV voltage is given by

$$\frac{\partial V_{pv}}{\partial I_{pv}} = -N_s v_{th}\left(\frac{1}{N_p I_{sc} - I_{pv}}\right) < 0. \tag{56}$$

Finally, it can be determined that the sign of the first term of the Lyapunov function is positive $\left(\partial S/\partial I_{pv}\right) > 0$.

It is assumed in this instance that $I_{pv} = I_l$, where the subsequent intricate cases are examined in detail.

Case 1. Considering $0 < U_{eq} + U_n < 1$, thus

$$\dot{x}_1 = \frac{dI_l}{dt} = \frac{1}{L}\left(V_{pv} - V_{out}\left(1 - U_{eq} - U_n\right)\right) = \frac{V_{out}}{L} U_n. \tag{57}$$
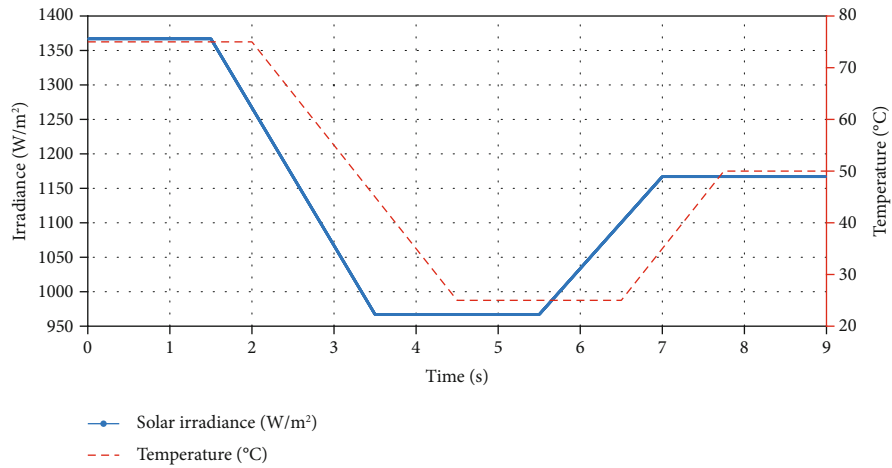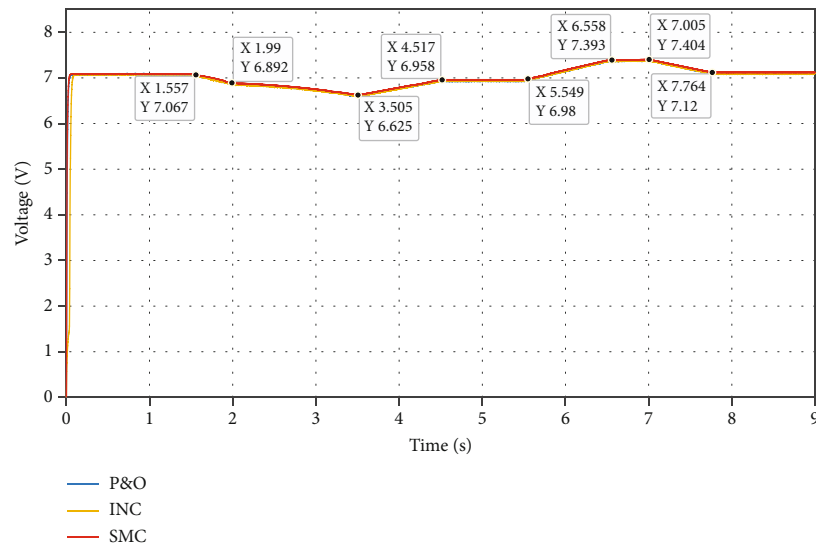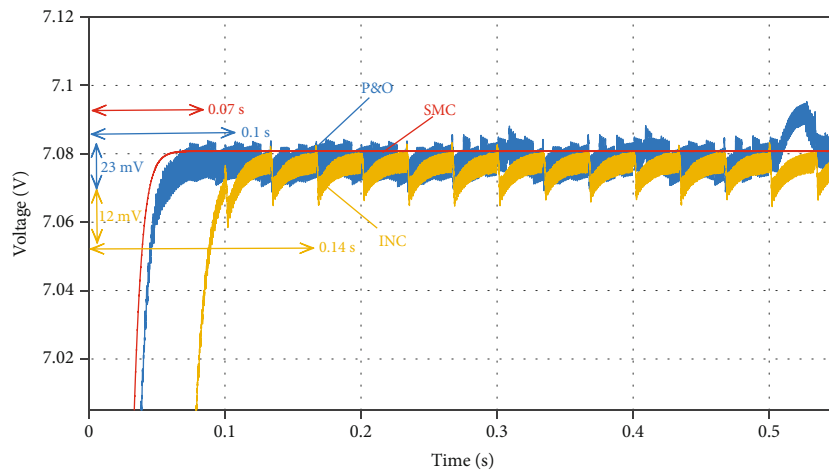
FIGURE 18: Solar irradiance and temperature variations: case 1 of EPS analysis.
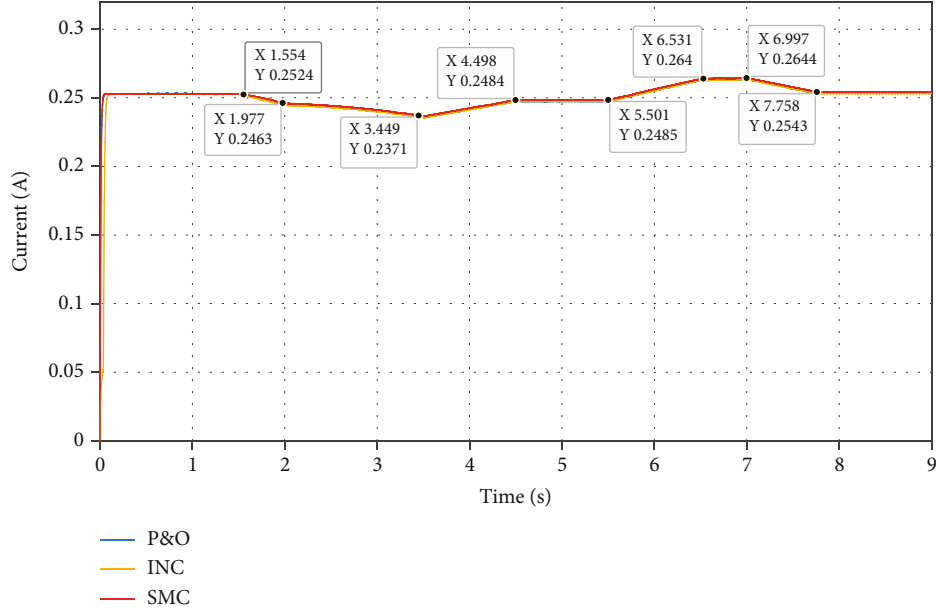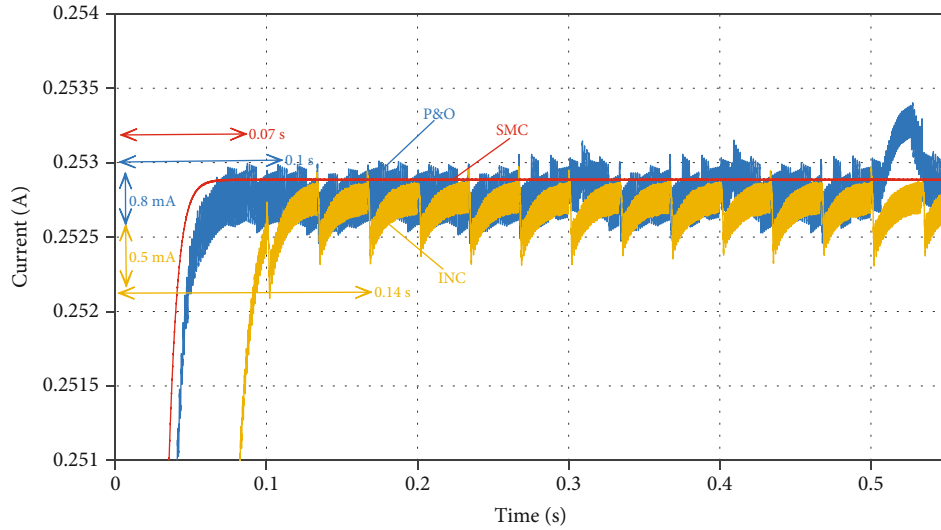

(a)

(b)

FIGURE 19: Boost power converter for 1 U solar panels (case 1 of EPS analysis): (a) output voltage comparison (P&O, INC, and SMC) and (b) zoom of output voltage comparison (P&O, INC, and SMC).

(a)

(b)

FIGURE 20: Boost power converter for 1 U solar panels (case 1 of EPS analysis): (a) output current comparison (P&O, INC, and SMC) and (b) zoom of output current comparison (P&O, INC, and SMC).

As previously stated and described, U_n is negative. Therefore, it is evident that the derivative of the surface $\dot{S}(x)$ is always of the opposite sign to the surface $S(x)$.

Case 2. Considering $U_{eq} + U_n = 1$, this means that $U_{eq} + U_n \geq 1$. Thus, based on the state of U_{eq}, two instances have to be examined.

If $U_{eq} = 1$, by (34), $V_{pv} = 0$. As seen in Figure 17, the surface $S(x)$ is positive in this instance. So, if $S(x) > 0$, the control input should be decreased. Consequently, $U_{eq} + U_n < 1$. But this contradicts the previously mentioned case $U_{eq} + U_n = 1$.

If both $U_{eq} < 1$ and $U_{eq} + U_n \geq 1$, $S(x) < 0$, then $S(x)\dot{S}(x) < 0$ is obtained.

It concludes that $S(x)\dot{S}(x) < 0$ for $U = 1$.

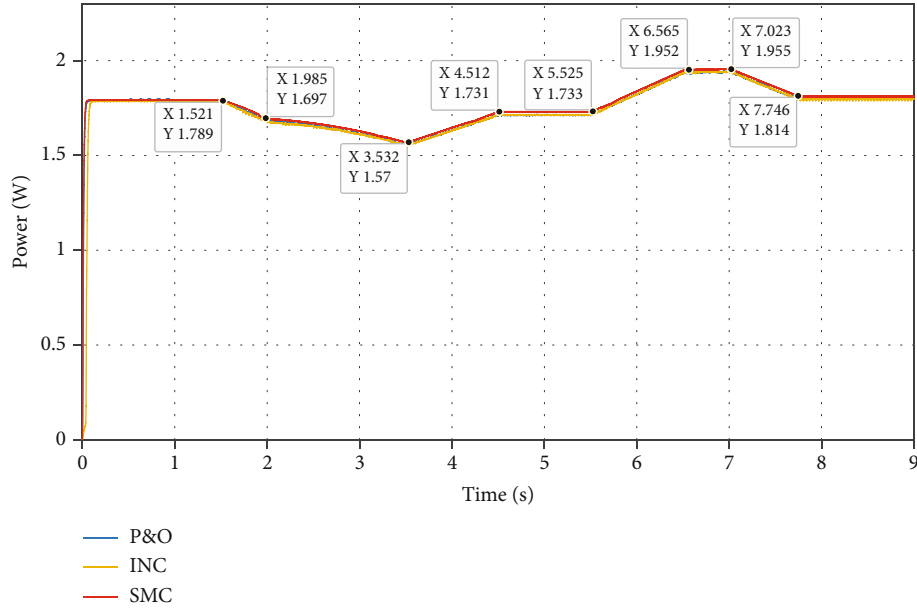Case 3. Considering $U_{eq} + U_n = 0$, which means that $U_{eq} + U_n \leq 0$ and

$$\dot{x}_1 = \frac{dI_l}{dt} = \frac{1}{L}\left(V_{pv} - V_{out}\right) < 0. \tag{58}$$

In this case, it is evident that $\dot{S}(x) < 0$. The two cases to check for the U_{eq} are as follows.
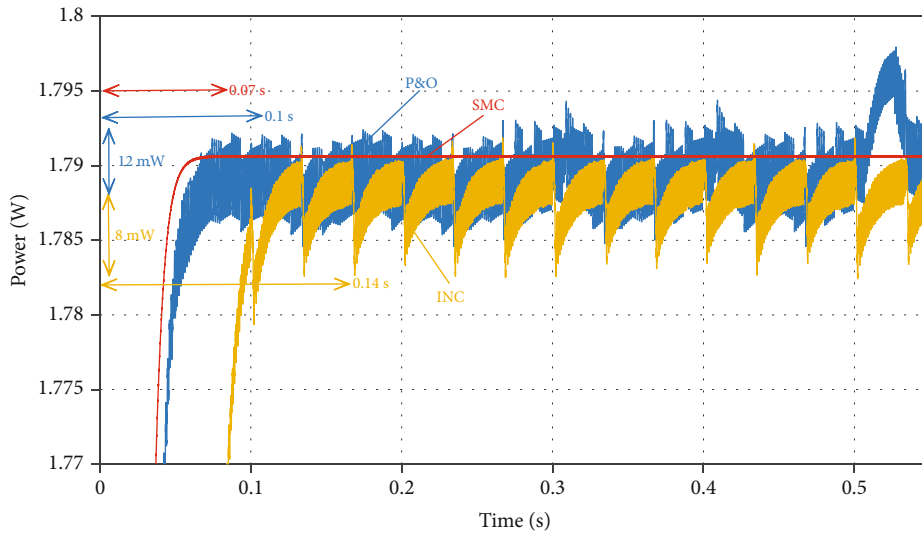
It follows that if

$$U_{eq} = 0, \tag{59}$$

$$V_{pv} = V_{out}. \tag{60}$$

(a)

(b)

FIGURE 21: Boost power converter with 1 U solar panel (case 1 of EPS analysis): (a) output power comparison (P&O, INC, and SMC) and (b) zoom of output power comparison (P&O, INC, and SMC).

From (59), it appears as though the PV array and the load are connected directly. Since the operating system is in the region where $S(x) < 0$, the duty cycle ought to go up in this situation. However, this opposes the case that $U_{eq} + U_n = 0$.

Consequently, when $U_{eq} > 0$ and $U_{eq} + U_n \leq 0$, $S(x) > 0$ is obtained for this case. After that, the state $\dot{x}_1 = dI_l/dt = 1/L(V_{pv} - V_{out}) < 0$ is examined.

From the above analysis, it can be concluded that stability is ensured since $S(x)$ and $\dot{S}(x)$ always have an opposite sign.

It is important to note that to prevent the controller from constantly saturating on the states of $U = 0$ or $U = 1$ without hitting the range of $0 < U < 1$, a suitable design should be used for the switching control U_n. Hence, in the
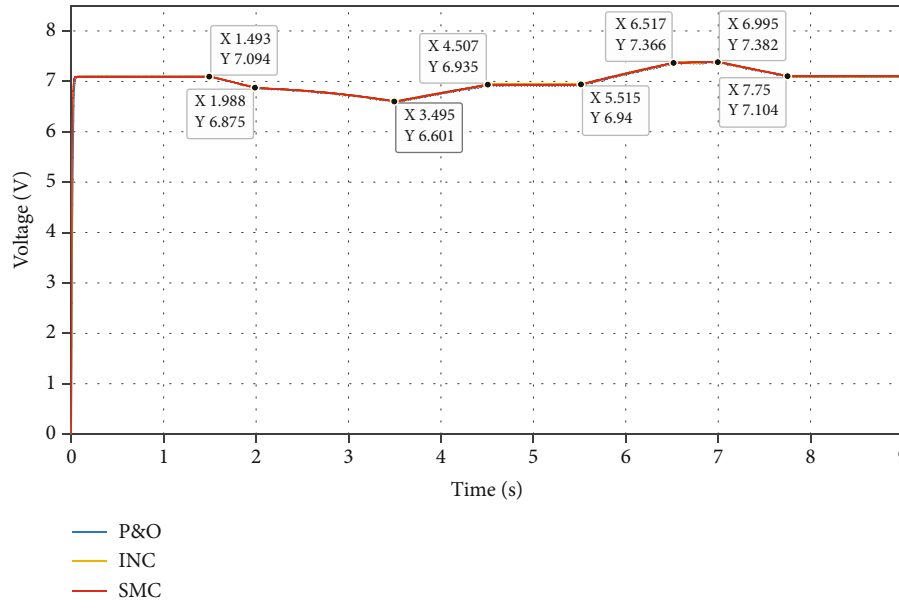
switching control U_n, the selection of the positive control gain K_{smc} often necessitates the fulfillment of the following condition:

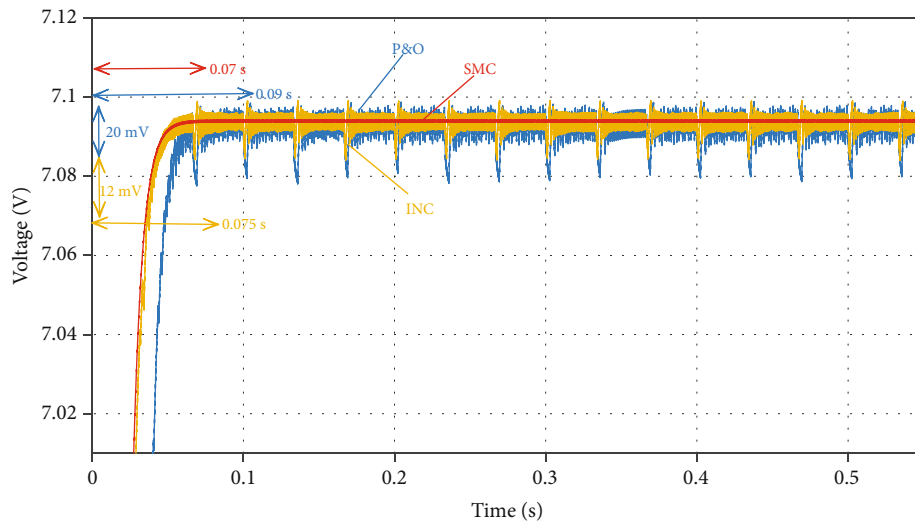$$K_{smc} \leq \frac{1}{|sign\ (S(x))|_{max}}. \tag{61}$$

This case is presented when $U_{eq} = 0$. Upon simplification, it is evident that

$$K_{smc} \leq 1. \tag{62}$$

Additionally, it is necessary to maintain the gain used by the switching control (U_n) at the minimum value to ensure

Figure 22: Buck power converter with 3 U solar panel (case 1 of EPS analysis): (a) output voltage comparison (P&O, INC, and SMC) and (b) zoom of output voltage comparison (P&O, INC, and SMC).

optimal performance of the controller. In order to reduce the impact of excessive chattering, it is advisable to utilize the smooth or saturation function instead of the sign function. The saturation function is employed in this paper for this reason.

It is possible to apply the Lyapunov stability analysis method to both buck and consistently boost power converters. The stability of the buck converter can be thoroughly examined thanks to the above method, which also simplifies the analytical process and helps with the design of a stable and robust SMC.

4. Simulation Results

In this section, the principle simulations are presented for the proposed EPS architecture for both 1 U and 3 U nanosa-

tellite platforms with the proposed MPPT control techniques. The electrical parameters of the EPS are shown in Appendix. The energy from the sun is the main source of power for the nanosatellite. However, there are other sources of irradiance in space (cosmic radiation, earth albedo, etc.), but only a few of them can be noteworthy. In this simulation, the Intel(R) Core(TM) i7-10750H CPU @ 2.60 GHz with a clock speed of 2.59 GHz is used to simulate the EPS model and control algorithms.

The simulation results presented in this paper investigate the dynamic responses of EPS under three distinct cases. In case 1, the effects of varying solar irradiance and temperature in ramp curves are examined. Case 2 involves the simulation of solar irradiance variation caused by attitude nanosatellite spinning. Lastly, in case 3, the response of EPS to nonuniform solar irradiance with added noise is
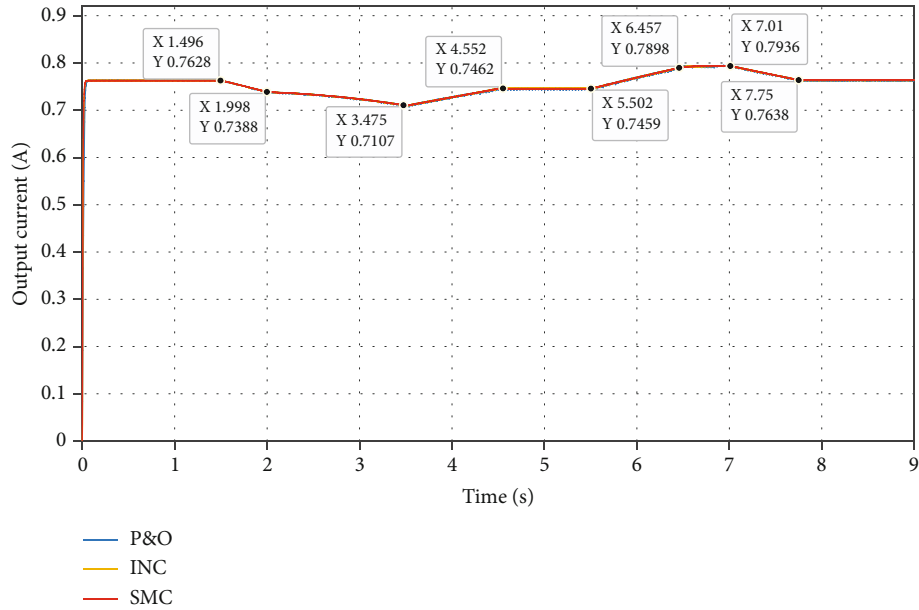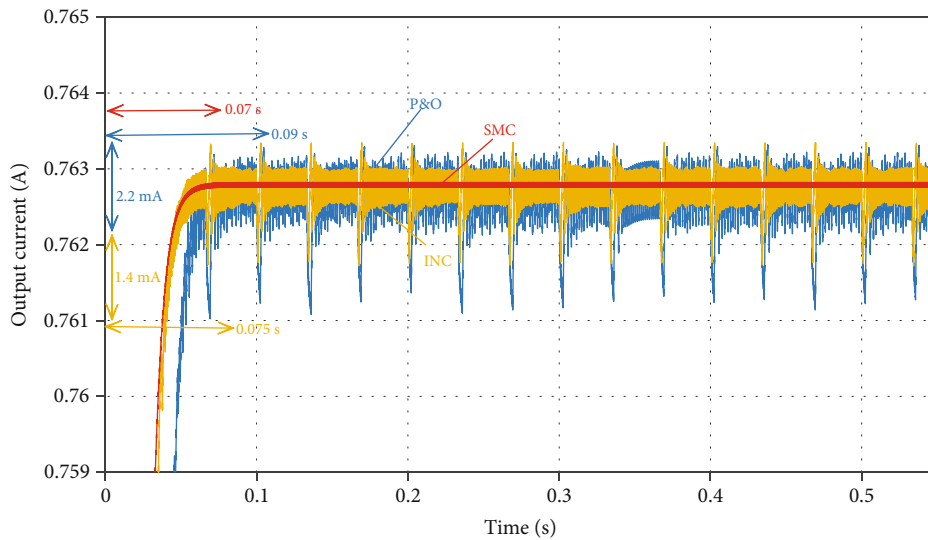
FIGURE 23: Buck power converter with 3 U solar panel (case 1 of EPS analysis): (a) output current comparison (P&O, INC, and SMC) and (b) zoom of output current comparison (P&O, INC, and SMC).

analyzed. These cases enable the exploration and understanding of the system's behavior under various dynamic environmental conditions.

4.1. Dynamic Response of EPS with MPPT Control Methods: Case 1.
In this case of simulation, the variations of temperature and the direct irradiance from the sun in orbit are considered as seen in Figure 18.

As seen in Figure 18, for the explicit expedition of the analysis of power system control strategies, the simulation is started with the temperature and solar irradiance constant from 0 to 1.5 seconds. Then, the temperature is maintained constant while the solar irradiance varies between 1.5 and 2 seconds. From 2 to 3.5 seconds, solar irradiance and tem-

perature drop to 967 W/m^2 and 45°C, respectively. While the temperature drops from 3.5 to 4.5 seconds to reach 25°C, the amount of sunlight irradiance remains constant. From 4.5 to 5.5 seconds, solar irradiance and temperature remained constant again. As the sun's irradiance reaches 1100 W/m^2, the temperature remains constant for 5.5 to 6.5 seconds. The sun's irradiance and temperature are both increasing, reaching 1167 W/m^2 and 35°C in 6.5 s to 7 seconds. The solar irradiance remains constant from 7 to 7.75 seconds as the temperature rises to 50°C. From 7.75 to 9 seconds, the solar irradiance and temperature are kept constant.

As previously described, the suggested EPS architectures for both 1 U and 3 U nanosatellite platforms employ boost and buck power converters connected to solar panels, their
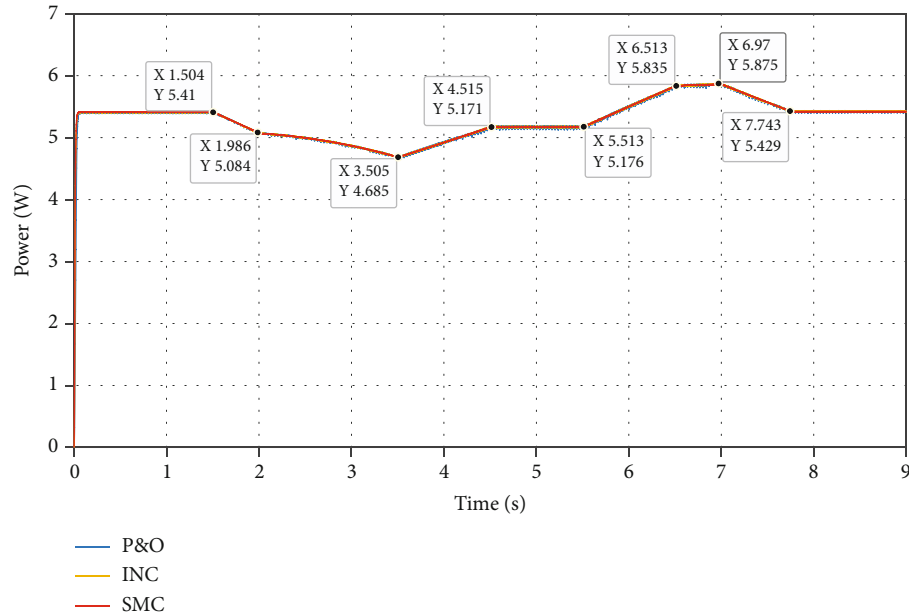
(a)
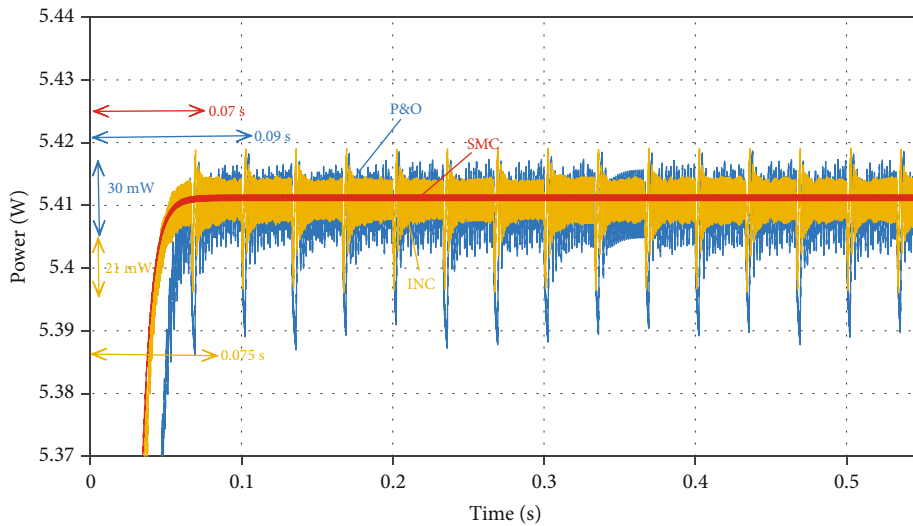
(b)

FIGURE 24: Buck power converter with 3 U solar panel (case 1 of EPS analysis): (a) output power comparison (P&O, INC, and SMC) and (b) zoom of output power comparison (P&O, INC, and SMC).

performances are proved by simulations, and the results are shown in the following subsections.

Figures 19–21 show a comparative analysis between the proposed control structure based on sliding mode control, and conventional control strategies based on P&O and INC, for the voltage, current, and power outputs and their capability to achieve MPPT characteristics in terms of overshoots, oscillations, and response time.

Figures 19(a) and 20(a) show that the voltage and current, obtained by control methods based on P&O, INC, and SMC, are varying according to the changes of the environmental conditions (solar irradiance and temperature). The voltages obtained by different control methods are achieving 7.4 V as the maximum and 6.62 V as the mini-

TABLE 3: Performance comparison of different MPPT algorithms.

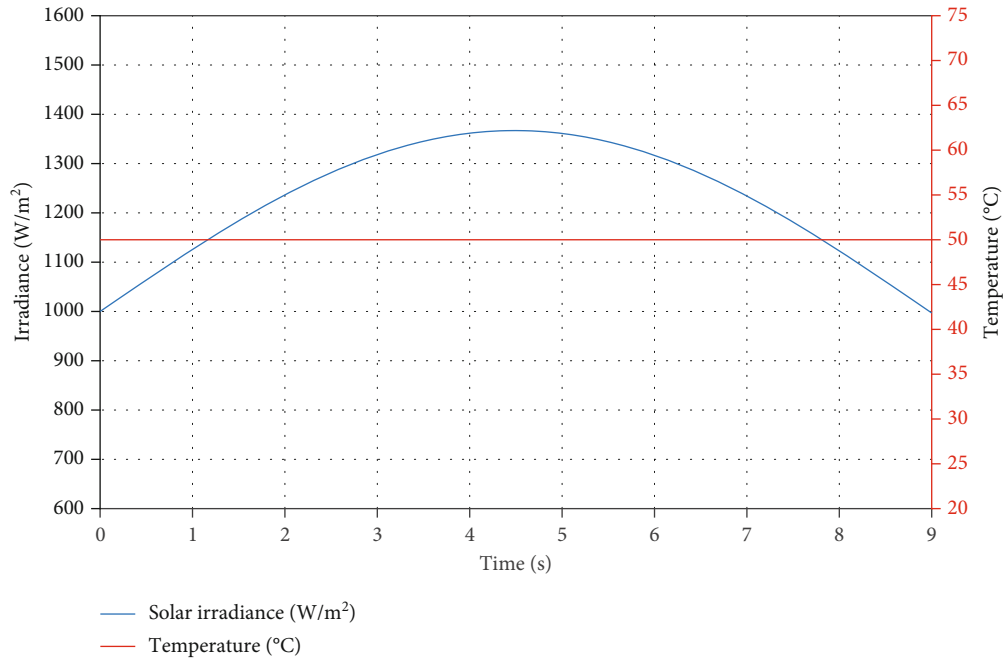|	Average power	Oscillation	Efficiency	Settling time
SMC (buck)	5.412	0.002	97%	0.07
P&O (buck)	5.4	0.03	96.4%	0.09
INC (buck)	5.411	0.02	96.6%	0.075
SMC (boost)	1.7905	0.001	98%	0.07
P&O (boost)	1.7895	0.009	97%	0.1
INC (boost)	1.77	0.008	96%	0.14

FIGURE 25: Solar irradiance and temperature variations: case 2 of EPS analysis.

mum. Whereas, the currents obtained by different control techniques are achieving 0.26 A as maximum and 0.23 A as minimum.

Figures 19(b) and 20(b) reveal how high- and low-frequency fluctuations appeared on the delivered current and voltage when employing the P&O and INC techniques. It can be noticed that the current and voltage obtained by the proposed method based on SMC have some significantly reduced fluctuations.

As depicted in Figure 21(a), the generated powers from the three MPPT control systems successfully tracked the MPP during variations in solar irradiance and temperature. At 1367 W/m^2 and 75°C, the PV powers produced by the SMC, P&O, and INC MPPT techniques are around 1.798 W same as that obtained during the PV characterization (see Figure 9). For other solar irradiances and temperatures, the generated power has a minimum of power of 1.57 W and a maximum of power of 1.955 W. However, as seen in Figure 21(b), oscillations were overlooked for SMC, 12 mW for P&O, and 8 mW for INC. The simulation shows also that at the same conditions of irradiance and temperature (1367 W/m^2 and 75°C), the settling times for SMC, P&O, and INC MPPT methods are 70 ms, 100 ms, and 140 ms, respectively.

Consequently, for the boost power converter with a 1 U solar panel, the proposed MPPT-based SMC algorithm demonstrates superior performance compared to the P&O and INC control methods. It exhibits precise reference tracking, minimal ripples, stability in steady-state operation, and enhanced efficiency with reduced losses.

In the EPS used for 3 U nanosatellite platforms, the buck power converters are used. Therefore, the comparative analysis between the proposed control theory based on sliding mode control and conventional control strategies based on

P&O and INC in terms of ripples, oscillations, and time response is demonstrated in Figures 22–24.

Figures 22(a) and 23(a) show that the voltage and current, attained by control methods based on P&O, INC, and SMC, vary according to the environmental conditions changes (solar irradiance and temperature). The voltages reached by different control methods achieved 7.38 V as the maximum and 6.6 V as the minimum, while the currents obtained by different control techniques are achieving 0.79 A as maximum and 0.71 A as minimum. It is interesting to note that the voltage and current time responses achieved using the SMC approach are faster than those obtained using the other MPPT control methods (Figures 22(a) and 23(a)).

As illustrated in Figure 24(a), the generated powers from the three MPPT control systems successfully tracked the MPP during variations in solar irradiance and temperature. At 1367 W/m^2 and 75°C, the PV powers produced by the SMC, P&O, and INC MPPT techniques are around 5.41 W same as that obtained during the PV characterization (see Figure 10). For other solar irradiances and temperatures, the generated power has a minimum of power of 4.685 W and a maximum of power of 5.875 W. However, as shown in Figure 24(b), there is the existence of oscillations of 30 mW for MPPT control using P&O, and 21 mW using the INC approach, where the oscillations of the output power using SMC are disregarded.

Table 3 shows a performance comparison of different MPPT methods.

These findings show that the generated powers produced using the recommended control technique based on SMC are more effective compared to the P&O and INC. This is because the other control methods are more susceptible to measurement disruptions and changes in the system's intrinsic features than the suggested SMC methodology is.
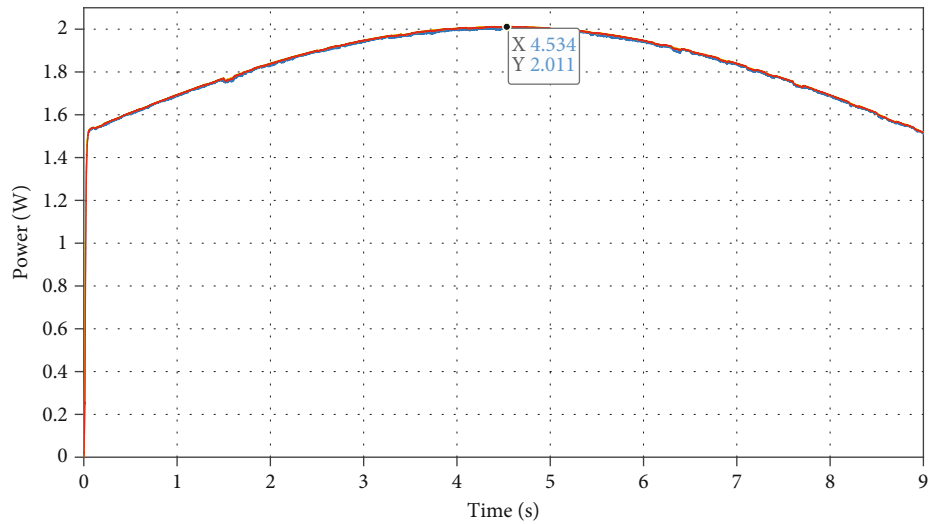
(a)
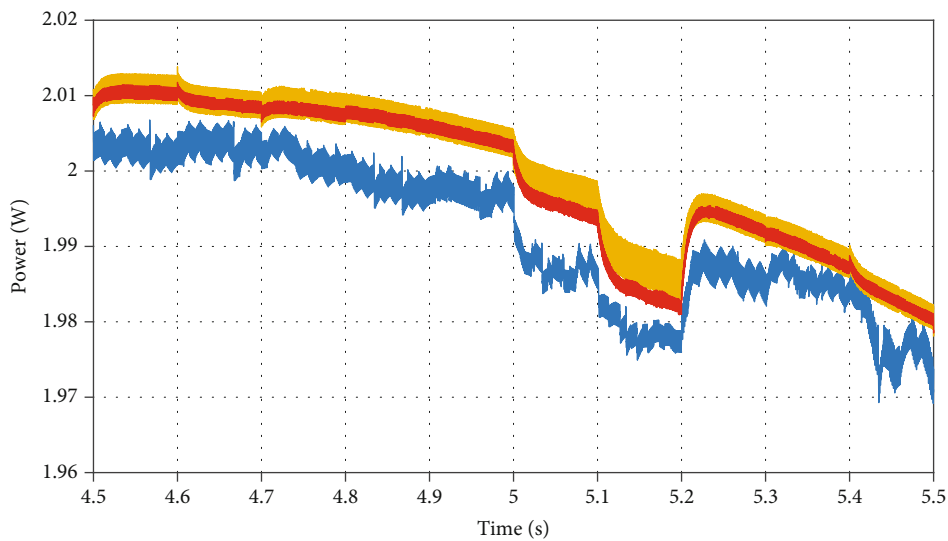
(b)

FIGURE 26: Boost power converter with 1 U solar panel (case 2 of EPS analysis): (a) output power comparison (P&O, INC, and SMC) and (b) zoom of output power comparison (P&O, INC, and SMC).

4.2. Dynamic Response of EPS with MPPT Control Methods: Case 2. In this simulation, the performance of the EPS with proposed methods on a 1 U nanosatellite and 3 U nanosatellite is examined, both rotating at a speed of 6.67 rpm and oriented toward the sun (sun-pointing orientation). The simulation takes into account the variations in direct irradiance and temperature, as depicted in Figure 25. These variations are essential in evaluating the effectiveness of the proposed methods under dynamic environmental conditions.

To simulate real experimental conditions, the voltage and current measurements utilized for the MPPT control methods experience disturbance by applying band-limited white noise. This disturbance has an amplitude of 0.002 and a sampling time of 0.1.

Figures 26(a) and 27(a) depict the changes in output power obtained from the solar PV panels when using solar irradiance data from case 2. The MPP varies in a similar pattern to the solar irradiance, indicating variations in the operating voltage and current.
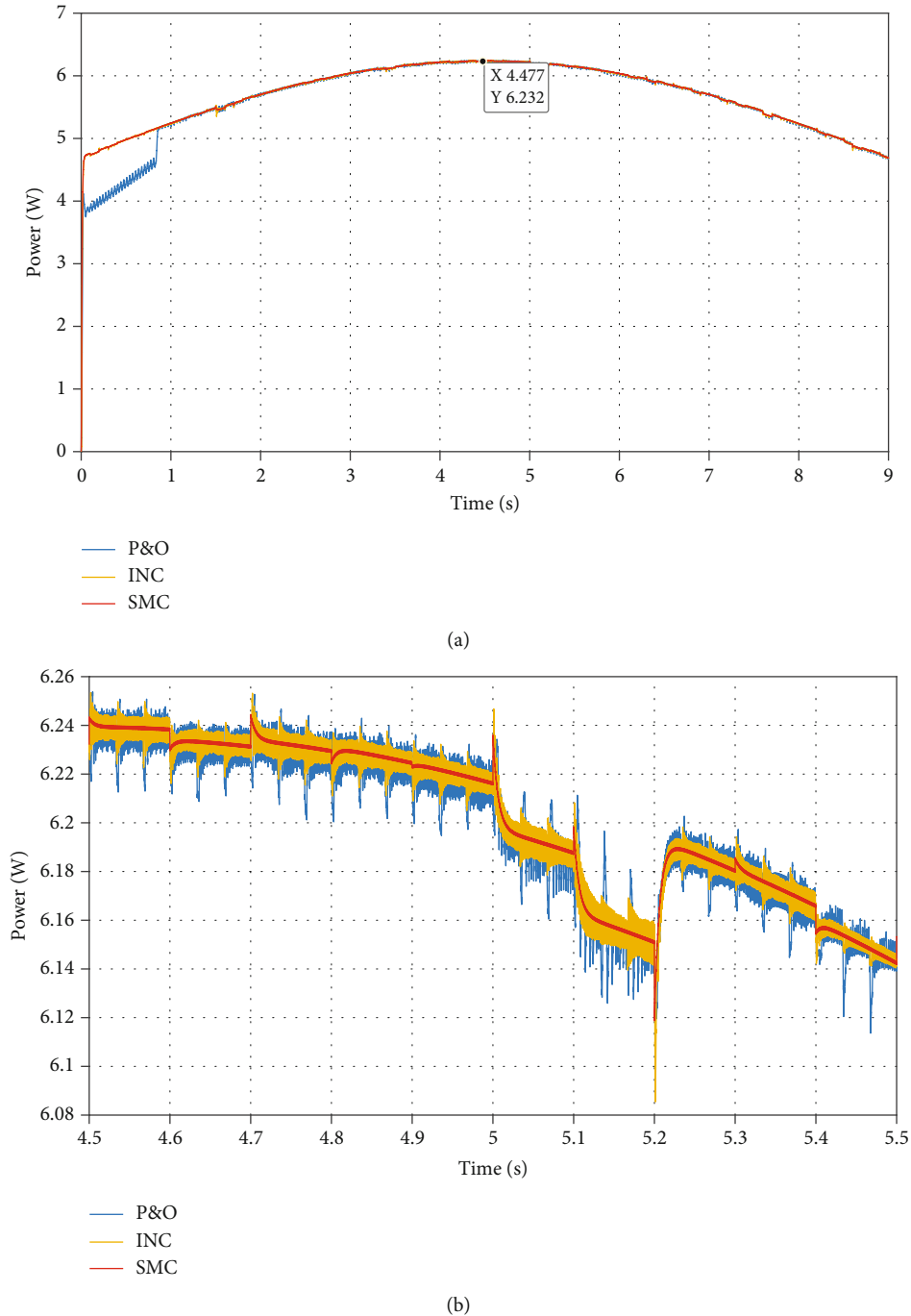
(a)

(b)

FIGURE 27: Buck power converter with 3 U solar panel (case 2 of EPS analysis): (a) output power comparison (P&O, INC, and SMC) and (b) zoom of output power comparison (P&O, INC, and SMC).

Additionally, Figure 26(b) shows that the SMC method significantly reduces oscillations to less than half (2 mW) compared to the P&O method, which exhibits oscillations of 7 mW, and the INC method, which shows oscillations of 5 mW (as indicated in Figure 26(b)). Similarly, for the buck power converter, as shown in Figure 27(b), the SMC method performs exceptionally well with minimal oscillations of 6 mW, while the P&O and INC methods exhibit high oscillations of approximately 42 mW and 31 mW, respectively.

In summary, when comparing the results obtained in case 1, the introduction of noise in voltage and current measurements in case 2 leads to nearly double the amplitude of oscillations.

4.3. Dynamic Response of EPS with MPPT Control Methods: Case 3. In this simulation scenario, the proposed methods are evaluated for two different nanosatellite platforms: a 1 U nanosatellite and a 3 U nanosatellite. Both nanosatellites
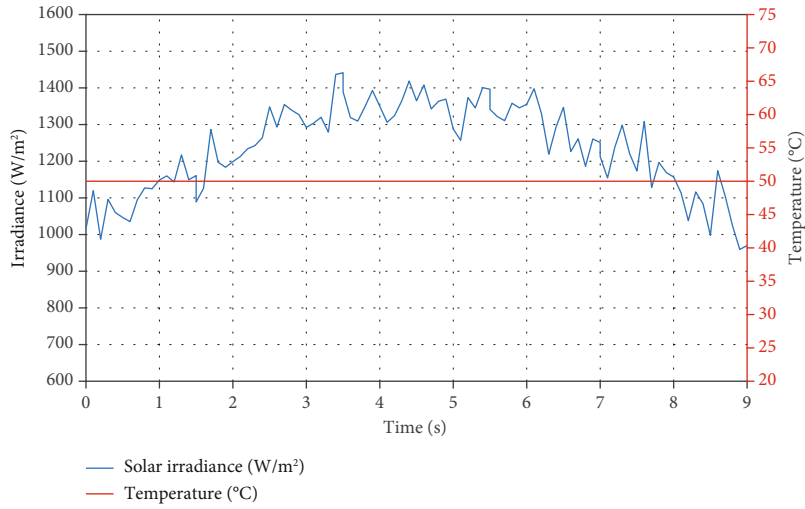
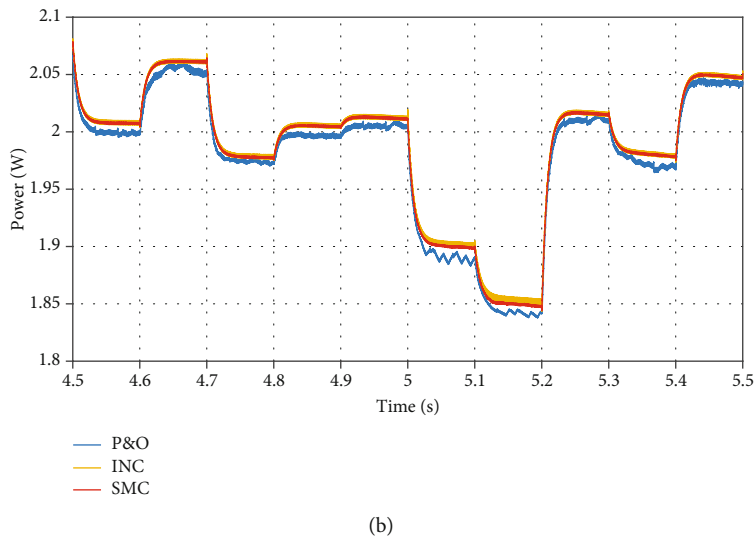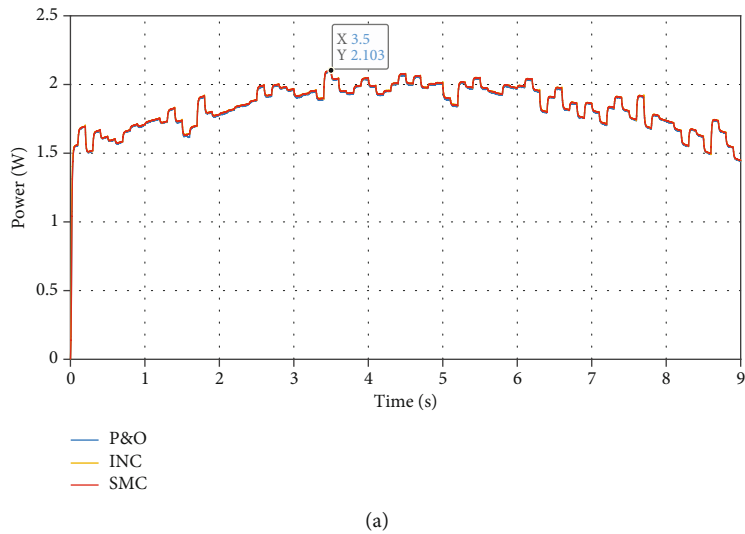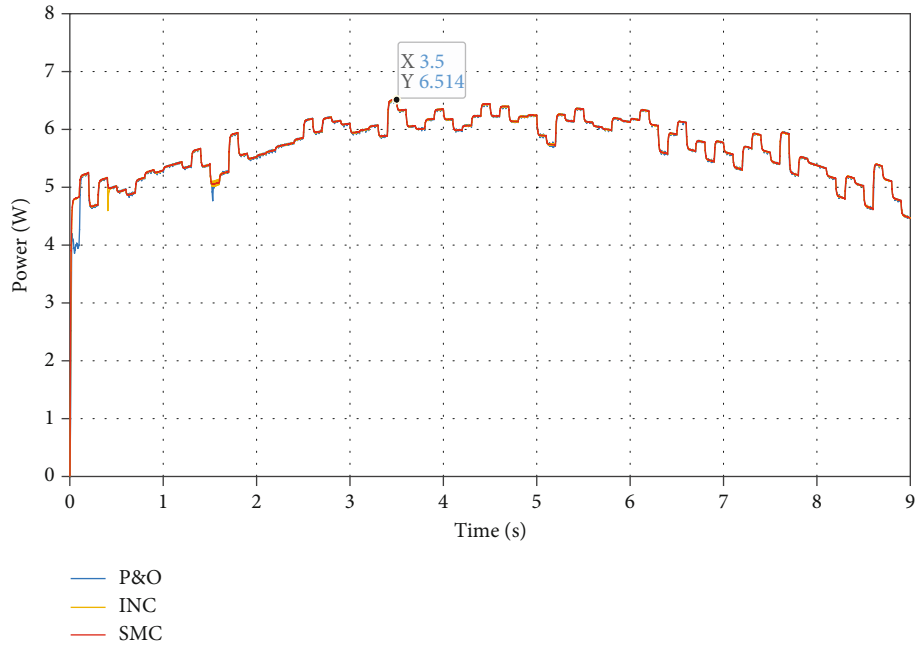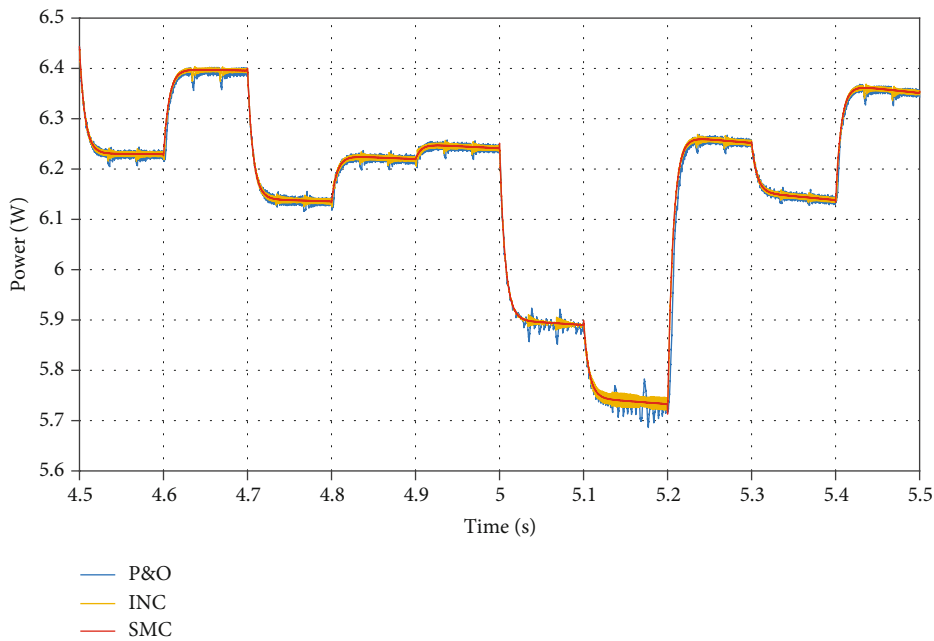FIGURE 28: Solar irradiance and temperature variations: case 3 of EPS analysis.

(a)

(b)

FIGURE 29: Boost power converter with 1 U solar panel (case 3 of EPS analysis): (a) output power comparison (P&O, INC, and SMC) and (b) zoom of output power comparison (P&O, INC, and SMC).

(a)

(b)

FIGURE 30: Buck power converter with 3 U solar panel (case 3 of EPS analysis): (a) output power comparison (P&O, INC, and SMC) and (b) zoom of output power comparison (P&O, INC, and SMC).

are configured to have the same spinning speed of 6.67 rpm and are oriented toward the sun (sun-pointing orientation). To accurately replicate real experimental conditions, the simulation takes into account nonuniform variations in direct irradiance, as depicted in Figure 28. These variations reflect the dynamic changes experienced by the nanosatellite throughout its mission.

Figures 29(a) and 30(a) reveal that the output power generated by the solar PV panels changes compared to the results obtained from case 1 and case 2. The MPP exhibits

changes that align with the pattern of solar irradiance variations, which can be attributed to fluctuations in operating voltage and current. In contrast, a closer examination of Figure 29(b) illustrates significantly reduced oscillations for the SMC method in power obtained by the boost power converter, with a mere 4 mW deviation.

Similarly, an analysis of Figure 30(b) illuminates a significant reduction in oscillations of about 6 mW obtained by SMC for power obtained by the buck power converter. Comparatively, in the same figure, the P&O method exhibits
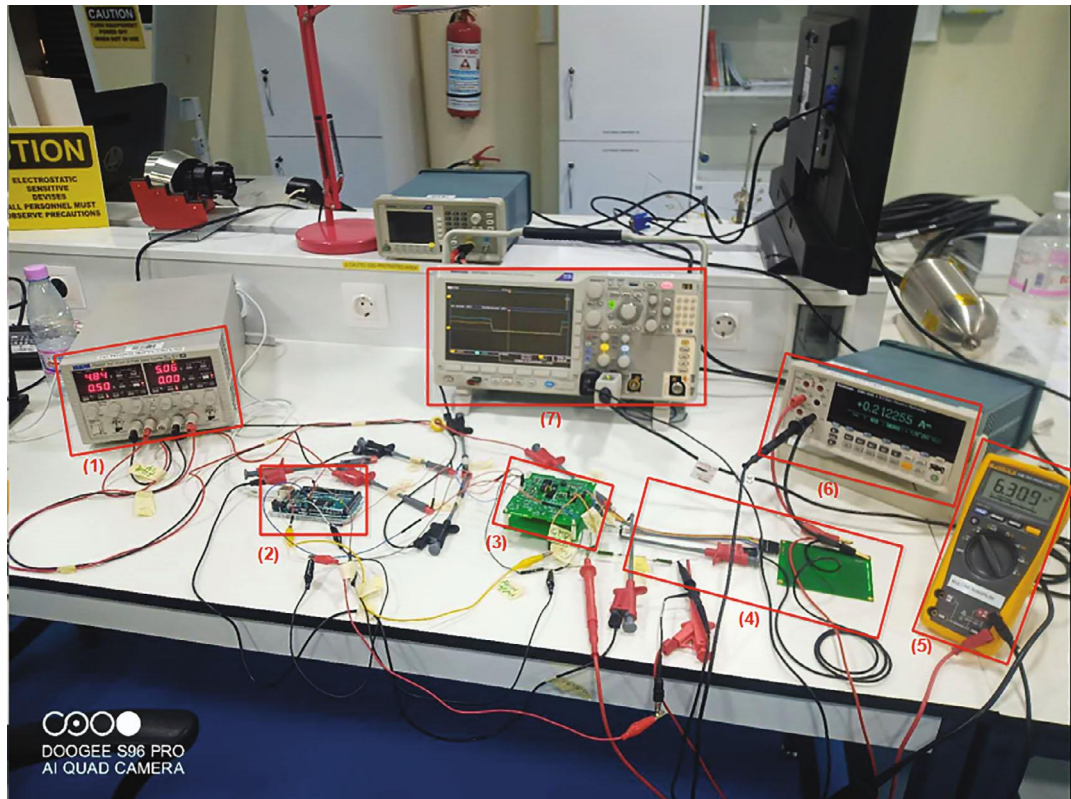
Figure 31: Experimentation bed for testing the power converters of the proposed EPS: (1) power supply and measurements, (2) MCU, (3) EPS (PRU), (4) electrical load, (5) voltmeter, (6) digital multimeter, and (7) oscilloscope.

oscillations of 92 mW, while the INC method shows oscillations of 36 mW (as depicted in Figure 30(b)). Compared to the results obtained in case 1, the oscillations are doubled in case 3 due to the introduction of noise in voltage and current measurements.

The results indicate that the SMC method is highly effective in minimizing power oscillations, outperforming the P&O and INC methods. The SMC method also performs well in terms of time response, compared to the other methods.

5. Experimental Results

The testing and experimental verification are illustrated in Figure 31, wherein the solar panel is substituted with an electrical programmable power supply connected to the designed EPS. This EPS is comprised of both boost and buck power converters sized to supply the load efficiently as described in the previous section. The MPPT control algorithms, crucial for optimizing power extraction from the solar panels, are implemented within a cost-effective microcontroller unit (MCU) based on Atmega 2560 from Microchip. This MCU has undergone thorough evaluation, demonstration, and validation for space environments and mission capabilities, as documented in [66, 67].

The upcoming experimental results will facilitate a comparative analysis of various MPPT control algorithms employed in conjunction with both boost and buck power converters.

The proposed testbed, which is also specifically designed for validating the functionality and sizing parameters of the power converters, is visually demonstrated in the accompanying figures of experimental results.

Initially, as shown in Figures 32–34, under low power generation conditions, the power output from a 3 U solar panel interfaced with the buck power converter is approximately three times higher than that of a 1 U solar panel connected to the boost power converter. Then, a comprehensive examination of power curves generated through experimental trials investigates into the nuanced performance of distinct MPPT algorithms—P&O, INC, and SMC. Within the specific setting of the boost converter, the power optimisation method is found to demonstrate a little superiority with SMC, followed by P&O, and INC. Significantly, a similar pattern can be observed in the context of the buck converter, where SMC occurs as the leading method for power optimization, with P&O, and INC following suit. These results offer valuable understanding on the efficacy of various MPPT methods in practical scenarios and emphasize the dependability of their performance in both experimental and simulated settings. Thus, based on the experimental conditions, the obtained results demonstrate that the SMC algorithm has a notable benefit in enhancing power extraction efficiency.

From simulation and experimentation, it is crucial to elucidate the factors contributing to the success of SMC. SMC operates by creating a sliding surface, essentially acting as a boundary within the system dynamics. In the context of
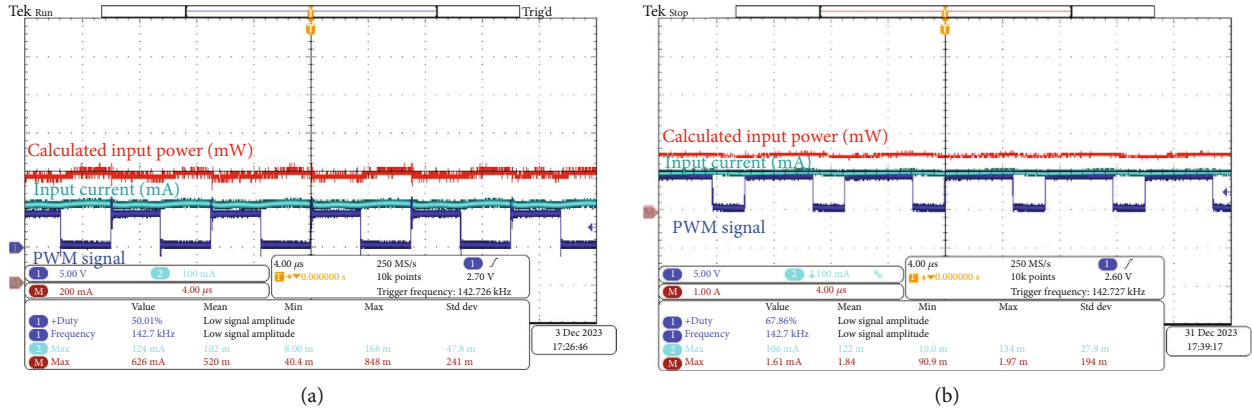
FIGURE 32: Measured responses (input power, input current, and control signal) with MPPT based on P&O: (a) boost power converter and (b) buck power converter.
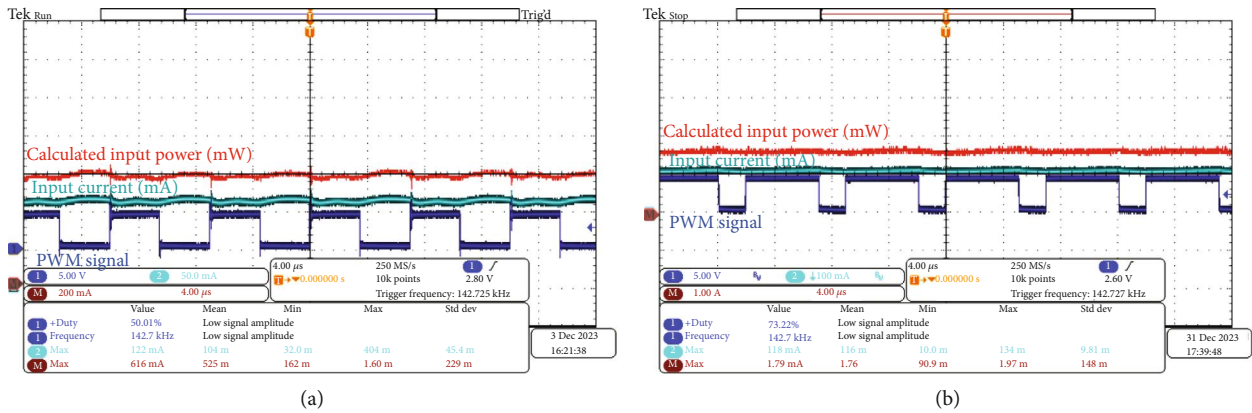
FIGURE 33: Measured responses (input power, input current, and control signal) with MPPT based on INC: (a) boost power converter and (b) buck power converter.
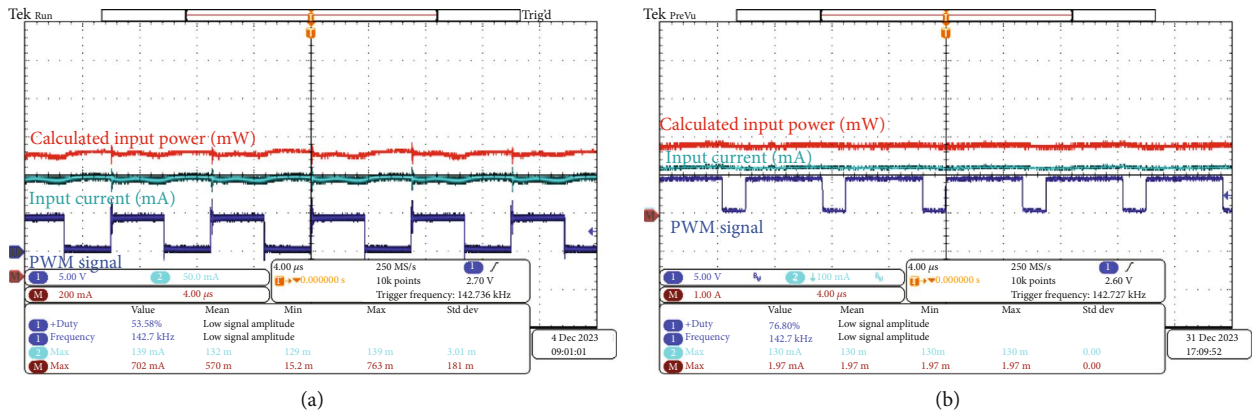
FIGURE 34: Measured responses (input power, input current, and control signal) with MPPT based on SMC: (a) boost power converter and (b) buck power converter.

MPPT for solar PV systems, this sliding surface is strategically designed to guide the operating point toward the MPP. The effectiveness of SMC lies in its ability to ensure that the system trajectory adheres to this surface, leading to rapid convergence and precise tracking of the MPP, even in the presence of uncertainties and variations in the system.

Notably, SMC overcomes the ripple issues compared to conventional methods like P&O and INC, resulting in a smoother and more stable control response. Furthermore, SMC exhibits intrinsic reliability, making it well-suited for practical scenarios characterized by varying environmental conditions and system parameters. Its dynamic response

Table 4: Electrical characteristics of AzurSpace 3G solar cells [68].

Open circuit voltage (V)	2.716
Short circuit current (mA)	17.5
Maximum power voltage (V)	2.427
Maximum power current (mA)	17.0
Maximum power (mW/cm^2)	41.14
Efficiency (%)	30.1

Table 5: Parameters of the boost power converter.

Inductor (mH)	2.716
Input capacitor (mF)	17.5
Output capacitor (mF)	2.427

Table 6: Parameters of the buck power converter.

Inductor (mH)	0.5
Input capacitor (uF)	70.5
Output capacitor (uF)	1.2

and adaptability significantly enhance energy harvesting efficiency, especially in challenging conditions such as nonuniform irradiance, where traditional approaches may encounter difficulties. Despite the requirement for careful tuning, the reliability of SMC in handling uncertainties and its exceptional performance features make it a highly attractive option for achieving optimal MPPT in EPS for nanosatellite platforms. This type of control algorithm can be easily implemented on low-cost and reliable microcontrollers for the application of nanosatellites that should avoid high calculation time and high power consumption of processors.

6. Conclusion

An electrical power system (EPS) architecture for two different platforms of nanosatellites (1 U and 3 U) is presented in this paper. Then, a brief comprehensive review of maximum power point tracking (MPPT) techniques used to ensure optimized power throughout the mission lifetime is provided. The improved MPPT control for the EPS via sliding mode control (SMC) theory is described in detail for both configurations embedded in 1 U and 3 U nanosatellite platforms. The photovoltaic panels of the nanosatellite experience dynamic variations in temperature and irradiance due to irregular orientation relative to the sun during its orbital trajectory. In light of these challenges, a suggested SMC is compared to other traditional control strategies. Simulation results indicate that the proposed SMC outperforms other strategies in handling environmental fluctuations such as temperature and solar irradiance. This technique consistently generates high-quality, efficient, and ripple-free output power, ensuring optimal performance under changing conditions. According to the results presented in this study, the voltage, current, and power outputs exhibit better MPPT characteristics with the suggested control theory based on sliding mode control as compared to P&O, including oscilla-

tions being overlooked, a quick settling time, and no steady-state error. Then, the proposed control theory has been successfully implemented and rigorously tested in a hardware setup. The results affirm its effectiveness and demonstrate its practical applicability in real function, validating its potential for enhancing the performance of the system under study.

Future research will focus on using GaN transistor technology to enhance power converter design to facilitate an important power increase. To evaluate this enhancement, hardware-in-the-loop experiments employing GaN transistors will be conducted to evaluate the system's performance in the emulated space environment. To increase energy collection capabilities, deployable solar panels will also be incorporated.

Appendix

In this paper, the solar cell parameters are presented in Table 4.

The parameters of the boost power converter are presented in Table 5.

The parameters of the buck power converter are presented in Table 6.

Data Availability

No underlying data was collected or produced in this study.

Conflicts of Interest

The authors declare that they have no conflicts of interest.

Acknowledgments

References

[1] H. Heidt, J. Puig-Suari, A. Moore, S. Nakasuka, and R. Twiggs, "CubeSat: a new generation of picosatellite for education and industry low-cost space experimentation," in *14TH Annual/USU Conference on Small Satellites*, Utah State University, 2000.

[2] E. Kulu, *Nanosatellites through 2020 and beyond*, 2021 CubeSat Developers Workshop, 2021.

[3] R. Bedington, X. Bai, E. Truong-Cao et al., "Nanosatellite experiments to enable future space-based QKD missions," *EPJ Quantum Technology*, vol. 3, no. 1, pp. 1–10, 2016.

[4] T. M. Lim, A. M. Cramer, J. E. Lumpp, and S. A. Rawashdeh, "A modular electrical power system architecture for small spacecraft," *IEEE Transactions on Aerospace and Electronic Systems*, vol. 54, no. 4, pp. 1832–1849, 2018.

[5] B. Johnston-Lemke, N. Orr, G. Bonin, and R. Zee, "Modular power system: enabling scalable missions for the 1w to 1kw range," in *27th Annual AIAA/USU. Conference on Small Satellites*, Utah State University, 2013.

[6] O. Khan, M. E. Moursi, H. Zeineldin, V. Khadkikar, and M. Al Hosani, "Comprehensive design and control methodology for DC-powered satellite electrical subsystem based on PV and battery," *IET Renewable Power Generation*, vol. 14, no. 12, pp. 2202–2210, 2020.

[7] M. Yaqoob, A. Lashab, J. C. Vasquez, J. M. Guerrero, M. E. Orchard, and A. D. Bintoudi, "A comprehensive review on small satellite microgrids," *IEEE Transactions on Power Electronics*, vol. 37, no. 10, pp. 12741–12762, 2022.

[8] A. Faiza and K. D. E. Kamel, *Design of electrical power system for low-cost ecological nanosatellite*, Oxford, 2019.

[9] J. Faujdar, D. K. Gautam, and V. Verma, "A new converter for common mode noise reduction for EPS of a nano satellite," in *2020 IEEE First International Conference on Smart Technologies for Power, Energy and Control (STPEC)*, Nagpur, India, 2020.

[10] A. Seddjar, K. D. E. Kerrouche, and L. Wang, "Simulation of the proposed combined fuzzy logic control for maximum power point tracking and battery charge regulation used in CubeSat," *Archives of Electrical Engineering*, vol. 69, 2020.

[11] E. Ilbis, *ESTCube-1 Electrical Power System–Design, Implementation and Testing*, Department of Science and Technology, University of Tartu, Tartu, Estonia, 2013.

[12] K. Kerrouche, L. Wang, and A. Aoudeche, "Low-cost EPS for nanosatellites constellation of belt and road countries," in *Fourth IAA Conference on Dynamics and Control of Space Systems*, DyCoSS, 2018.

[13] A. Aoudeche, X. Zhao, and K. D. Kerrouche, "Design of a high performance electrical power system for an earth observation nano-satellite," in *Proceedings of the 2018 international conference on electronics and electrical engineering technology*, pp. 140–146, Tianjin, China, 2018.

[14] M. F. N. Tajuddin, M. Arif, S. Ayob, and Z. Salam, "Perturbative methods for maximum power point tracking (MPPT) of photovoltaic (PV) systems: a review," *International Journal of Energy Research*, vol. 39, no. 9, pp. 1153–1178, 2015.

[15] M. F. Jalil, S. Khatoon, I. Nasiruddin, and R. Bansal, "Review of PV array modelling, configuration and MPPT techniques," *International Journal of Modelling and Simulation*, vol. 42, no. 4, pp. 533–550, 2022.

[16] R. B. Bollipo, S. Mikkili, and P. K. Bonthagorla, "Hybrid, optimal, intelligent and classical PV MPPT techniques: a review," *CSEE Journal of Power and Energy Systems*, vol. 7, no. 1, pp. 9–33, 2020.

[17] R. Khan, L. Khan, S. Ullah, I. Sami, and J.-S. Ro, "Backstepping based super-twisting sliding mode MPPT control with differential flatness oriented observer design for photovoltaic system," *Electronics*, vol. 9, no. 9, p. 1543, 2020.

[18] B. Pakkiraiah and G. D. Sukumar, "Research survey on various MPPT performance issues to improve the solar PV system efficiency," *Journal of Solar Energy*, vol. 2016, Article ID 8012432, 20 pages, 2016.

[19] A. K. Abdelsalam, A. M. Massoud, S. Ahmed, and P. N. Enjeti, "High-performance adaptive perturb and observe MPPT technique for photovoltaic-based microgrids," *IEEE Transactions on Power Electronics*, vol. 26, no. 4, pp. 1010–1021, 2011.

[20] J. Ahmed and Z. Salam, "An improved perturb and observe (P&O) maximum power point tracking (MPPT) algorithm for higher efficiency," *Applied Energy*, vol. 150, pp. 97–108, 2015.

[21] N. Femia, G. Petrone, G. Spagnuolo, and M. Vitelli, "Optimization of perturb and observe maximum power point tracking method," *IEEE Transactions on Power Electronics*, vol. 20, no. 4, pp. 963–973, 2005.

[22] F. Liu, S. Duan, F. Liu, B. Liu, and Y. Kang, "A variable step size INC MPPT method for PV systems," *IEEE Transactions on Industrial Electronics*, vol. 55, pp. 2622–2628, 2008.

[23] P. Sivakumar, A. A. Kader, Y. Kaliavaradhan, and M. Arutchelvi, "Analysis and enhancement of PV efficiency with incremental conductance MPPT technique under nonlinear loading conditions," *Renewable Energy*, vol. 81, pp. 543–550, 2015.

[24] K. S. Tey and S. Mekhilef, "Modified incremental conductance MPPT algorithm to mitigate inaccurate responses under fast-changing solar irradiation level," *Solar Energy*, vol. 101, pp. 333–342, 2014.

[25] D.-Y. Lee, H.-J. Noh, D.-S. Hyun, and I. Choy, "An improved MPPT converter using current compensation method for small scaled PV-applications," in *Eighteenth Annual IEEE Applied Power Electronics Conference and Exposition, 2003. APEC '03*, pp. 540–545, Miami Beach, FL, USA, 2003.

[26] H. A. Sher, A. F. Murtaza, A. Noman, K. E. Addoweesh, and M. Chiaberge, "An intelligent control strategy of fractional short circuit current maximum power point tracking technique for photovoltaic applications," *Journal of Renewable and Sustainable Energy*, vol. 7, no. 1, 2015.

[27] C. B. N. Fapi, P. Wira, M. Kamta, H. Tchakounté, and B. Colicchio, "Simulation and dSPACE hardware implementation of an improved fractional short-circuit current MPPT algorithm for photovoltaic system," *Applied Solar Energy*, vol. 57, no. 2, pp. 93–106, 2021.

[28] K. Kobayashi, H. Matsuo, and Y. Sekine, "A novel optimum operating point tracker of the solar cell power supply system," in *2004 IEEE 35th Annual Power Electronics Specialists Conference (IEEE Cat. No.04CH37551)*, pp. 2147–2151, Aachen, Germany, 2004.

[29] D. Baimel, S. Tapuchi, Y. Levron, and J. Belikov, "Improved fractional open circuit voltage MPPT methods for PV systems," *Electronics*, vol. 8, no. 3, p. 321, 2019.

[30] A. Mehiri, M. Bettayeb, A.-K. Hamid, and A. Ardjal, "Fractional nonlinear synergetic control for DC-link voltage regulator of three phase inverter grid-tied PV system," in *2018 5th International Conference on Renewable Energy: Generation and Applications (ICREGA)*, pp. 90–93, Al Ain, United Arab Emirates, 2018.

[31] S. Sajadian, "Power optimizer based on model predictive control for a cascaded multilevel impedance source inverter," in *2020 IEEE Energy Conversion Congress and Exposition (ECCE)*, pp. 99–104, Detroit, MI, USA, 2020.

[32] R. Arulmurugan and N. Suthanthiravanitha, "Model and design of a fuzzy-based Hopfield NN tracking controller for standalone PV applications," *Electric Power Systems Research*, vol. 120, pp. 184–193, 2015.

[33] H. Rezk, M. Aly, M. Al-Dhaifallah, and M. Shoyama, "Design and hardware implementation of new adaptive fuzzy logic-based MPPT control method for photovoltaic applications," *IEEE Access*, vol. 7, pp. 106427–106438, 2019.

[34] M. Farhat, O. Barambones, and L. Sbita, "Efficiency optimization of a DSP-based standalone PV system using a stable single input fuzzy logic controller," *Renewable and Sustainable Energy Reviews*, vol. 49, pp. 907–920, 2015.

[35] H. Boumaaraf, A. Talha, and O. Bouhali, "A three-phase NPC grid-connected inverter for photovoltaic applications using neural network MPPT," *Renewable and Sustainable Energy Reviews*, vol. 49, pp. 1171–1179, 2015.

[36] A. K. Rai, N. Kaushika, B. Singh, and N. Agarwal, "Simulation model of ANN based maximum power point tracking controller for solar PV system," *Solar Energy Materials and Solar Cells*, vol. 95, no. 2, pp. 773–778, 2011.

[37] M. M. Savrun and M. İnci, "Adaptive neuro-fuzzy inference system combined with genetic algorithm to improve power extraction capability in fuel cell applications," *Journal of Cleaner Production*, vol. 299, p. 126944, 2021.

[38] A. Elsheikh and M. Abd Elaziz, "Review on applications of particle swarm optimization in solar energy systems," *International journal of Environmental Science and Technology*, vol. 16, no. 2, pp. 1159–1170, 2019.

[39] A. M. Eltamaly, M. Al-Saud, A. G. Abokhalil, and H. M. Farh, "Simulation and experimental validation of fast adaptive particle swarm optimization strategy for photovoltaic global peak tracker under dynamic partial shading," *Renewable and Sustainable Energy Reviews*, vol. 124, article 109719, 2020.

[40] A. Sedaghat, M. Karami, and M. Eslami, "Improving performance of a photovoltaic panel by pin fins: a theoretical analysis," *Transactions of Mechanical Engineering*, vol. 44, no. 4, pp. 997–1004, 2020.

[41] L.-P. Liu, Z.-M. Fu, and X.-N. Song, "Tracking control of a class of differential inclusion systems via sliding mode technique," *International Journal of Automation and Computing*, vol. 11, no. 3, pp. 308–312, 2014.

[42] Q. Xu, "Enhanced discrete-time sliding mode strategy with application to piezoelectric actuator control," *IET Control Theory & Applications*, vol. 7, no. 18, pp. 2153–2163, 2013.

[43] A. M. Othman, "Enhancement of tidal generators by superconducting energy storage and Jaya-based sliding-mode controller," *International Journal of Energy Research*, vol. 44, no. 14, pp. 11658–11675, 2020.

[44] K. Kerrouche, L. Wang, A. Mezouar, L. Boumediene, and A. Van Den Bossche, "Fractional-order sliding mode control for D-STATCOM connected wind farm based DFIG under voltage unbalanced," *Arabian Journal for Science and Engineering*, vol. 44, no. 3, pp. 2265–2280, 2019.

[45] M. B. Anjum, Q. Khan, S. Ullah et al., "Maximum power extraction from a standalone photo voltaic system via neuro-adaptive arbitrary order sliding mode control strategy with high gain differentiation," *Applied Sciences*, vol. 12, no. 6, p. 2773, 2022.

[46] M. Bjaoui, B. Khiari, R. Benadli, M. Memni, and A. Sellami, "Practical implementation of the backstepping sliding mode controller MPPT for a PV-storage application," *Energies*, vol. 12, no. 18, p. 3539, 2019.

[47] I.-S. Kim, "Robust maximum power point tracker using sliding mode controller for the three-phase grid-connected photovoltaic system," *Solar Energy*, vol. 81, no. 3, pp. 405–414, 2007.

[48] E. Bianconi, J. Calvente, R. Giral et al., "A fast current-based MPPT technique employing sliding mode control," *IEEE Transactions on Industrial Electronics*, vol. 60, no. 3, pp. 1168–1178, 2012.

[49] A. Ali, K. Almutairi, S. Padmanaban et al., "Investigation of MPPT techniques under uniform and non-uniform solar irradiation condition–a retrospection," *IEEE Access*, vol. 8, pp. 127368–127392, 2020.

[50] P. K. Pathak, A. K. Yadav, and P. Alvi, "Advanced solar MPPT techniques under uniform and non-uniform irradiance: a comprehensive review," *Journal of Solar Energy Engineering*, vol. 142, no. 4, article 040801, 2020.

[51] A. D. Martin, J. R. Vazquez, and J. Cano, "MPPT in PV systems under partial shading conditions using artificial vision," *Electric Power Systems Research*, vol. 162, pp. 89–98, 2018.

[52] L. E. P. Chenche, O. S. H. Mendoza, and E. P. Bandarra Filho, "Comparison of four methods for parameter estimation of mono- and multi-junction photovoltaic devices using experimental data," *Renewable and Sustainable Energy Reviews*, vol. 81, pp. 2823–2838, 2018.

[53] L. Zhang, P. Niu, Y. Li et al., "Investigation on high-efficiency Ga0. 51In0. 49P/In0. 01Ga0. 99As/Ge triple-junction solar cells for space applications," *AIP Advances*, vol. 7, no. 12, p. 125217, 2017.

[54] K. D. E. Kerrouche, A. Seddjar, N. Khorchef, S. A. Bendoukha, L. Wang, and A. Aoudeche, "CubeSat project: experience gained and design methodology adopted for a low-cost electrical power system," *Automatika*, vol. 63, no. 4, pp. 695–717, 2022.

[55] A. Seddjar, K. D. E. Kerrouche, F. Arezki, and N. Khorchef, "Comprehensive review of maximum power point tracking techniques and proposed fuzzy logic controller of an electrical power system for nano satellites," *Revue Roumaine Des Sciences Techniques—Série Électrotechnique Et Énergétique*, vol. 67, no. 2, pp. 123–131, 2022.

[56] A. Seddjar, K. D. E. Kerrouche, and N. Khorchef, "Power system topology proposal of a high-altitude pseudo-satellite: sizing method, power budget modeling and efficient power control," *Advances in Electrical and Computer Engineering*, vol. 22, no. 1, pp. 47–56, 2022.

[57] M. H. Rashid, *Power Electronics Handbook*, Butterworth-heinemann, 2011.

[58] T. Terras, S. Hadjeri, A. Mezouar, and T. Chikouche, "Robust speed control with rotor resistance estimation," *Canadian Journal of Electrical and Computer Engineering*, vol. 36, no. 2, pp. 43–51, 2013.

[59] K. D. E. Kerrouche, A. Mezouar, L. Boumediene, and A. Van Den Bossche, "Modeling and Lyapunov-designed based on adaptive gain sliding mode control for wind turbines," *Journal of Power Technologies*, vol. 96, pp. 124–136, 2016.

[60] S. Ahmad, A. A. Uppal, M. R. Azam, and J. Iqbal, "Chattering free sliding mode control and state dependent Kalman filter design for underground gasification energy conversion process," *Electronics*, vol. 12, no. 4, p. 876, 2023.

[61] K. D. E. Kerrouche, A. Mezouar, L. Boumediene, and A. Van Den Bossche, "A comprehensive review of LVRT capability and sliding mode control of grid-connected wind-turbine-driven doubly fed induction generator," *Automatika: Časopis Za Automatiku, Mjerenje, Elektroniku, Računarstvo I Komunikacije*, vol. 57, no. 4, pp. 922–935, 2016.

[62] J.-J. E. Slotine and W. Li, *Applied Nonlinear Control vol. 199*, Prentice hall Englewood, Cliffs, NJ, 1991.

[63] K. D. E. Kerrouche, L. Wang, A. Van Den Bossche, A. Draou, A. Mezouar, and L. Boumediene, "Dual robust control of grid-connected DFIGs-based wind-turbine-systems under unbalanced grid voltage conditions," in *Stability control and reliable performance of wind turbines*, IntechOpen Limited, London, 2018.

[64] E. A. J. Brea, E. I. Ortiz-Rivera, A. Salazar-Llinas, and J. Gonzalez-Llorente, "Simple photovoltaic solar cell dynamic sliding mode controlled maximum power point tracker for battery charging applications," in *2010 Twenty-Fifth Annual IEEE Applied Power Electronics Conference and Exposition (APEC)*, pp. 666–671, Palm Springs, CA, USA, 2010.

[65] R. Garraoui, M. Ben Hamed, and L. Sbita, "A robust optimization technique based on first order sliding mode approach for photovoltaic power systems," *International Journal of Automation and Computing*, vol. 12, no. 6, pp. 620–629, 2015.

[66] Y. Nurgizat, A.-A. Ayazbay, D. Galayko, G. Balbayev, and K. Alipbayev, "Low-cost orientation determination system for CubeSat based solely on solar and magnetic sensors," *Sensors*, vol. 23, no. 14, p. 6388, 2023.

[67] T. Kameda, A. Nagata, Y. Kimura et al., "Space environment evaluation and low-earth-orbit demonstration of a communication component with a commercial transceiver integrated circuit," *Aerospace*, vol. 9, no. 6, p. 280, 2022.

[68] P. Thirion, *Design and implementation of on-board electrical power supply of student nanosatellite OUFTI-1 of University of Liège*, Master in Electrical Engineering, Applied Science Faculty of the University of Liège, Liège, Belgium, 2009.